

# Three-Dimensional Forest Biophysical Measurement in Northern China (ForBio\_3D 2020-2023)

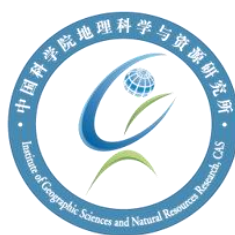
Field Measurement Report

Version 1.0

Hongliang Fang, Yu Li, Sijia Li, Yao Wang, Tian Ma, Yunjia Wu, Keruo  
Guo

State Key Laboratory of Resources and Environmental Information System,  
Institute of Geographic Sciences and Natural Resources Research,  
Chinese Academy of Sciences

November 2023



## Participants

Prof. Hongliang Fang

Principle Investigator

LREIS, Institute of Geographic Sciences and Natural Resources Research

Chinese Academy of Sciences

Beijing 100101, China

Email: [fanghl@lreis.ac.cn](mailto:fanghl@lreis.ac.cn)

Date	Site	Participants
September 2020	Saihanba National Forest Park	Yinghui Zhang, Yao Wang, Sijia Li
September 2020	Changbai Mountain	Yinghui Zhang, Yao Wang, Sijia Li, Tian Ma
April 2021	Saihanba National Forest Park	Lu Xu, Yao Wang, Sijia Li, Tian Ma
June 2021	Saihanba National Forest Park	Yinghui Zhang, Yao Wang, Sijia Li, Tian Ma, Yu Li
September 2021	Saihanba National Forest Park	Yao Wang, Sijia Li, Tian Ma, Yu Li, Kehong Hu
August 2022	Saihanba National Forest Park	Sijia Li, Yu Li, Yunjia Wu
September 2022	Changbai Mountain	Sijia Li, Yu Li, Yunjia Wu
April 2023	Saihanba National Forest Park	Yunjia Wu, Sijia Li, Yu Li
May 2023	Changbai Mountain	Yunjia Wu, Sijia Li, Yu Li
August 2023	Saihanba National Forest Park	Yunjia Wu, Yu Li, Keruo Guo
September 2023	Changbai Mountain	Yunjia Wu, Yu Li, Keruo Guo

LREIS, Institute of Geographic Sciences and Natural Resources Research  
 Chinese Academy of Sciences  
 Beijing 100101, China

## Acknowledgments

This study was mainly supported by the National Natural Science Foundation of China (42171358) and the National Key Research and Development Program of China (2016YFA0600201) to Hongliang Fang. Logistic support and accommodation were facilitated by the Saihanba Station of the Peking University Observatory System for Ecology and the Environment and the Research Station of Changbai Mountain Forest Ecosystems, Chinese Academy of Sciences. We thank the station manager Mr. Dai Guanhua for operating the crane tower and Dr. Sun Jian from Jilin University for providing geolocation during the measurement in Changbai Mountain.



**中华人民共和国科学技术部**  
Ministry of Science and Technology of the People's Republic of China

## Revision History

<i>Revision Date</i>	<i>Changes</i>	<i>Major contributor</i>
2022-10-14	Initial draft	Yu Li
2022-10-17	Major revision	Hongliang Fang
2023-07-10	Added 04-05/2023 field measurements	Yunjia Wu
2023-09-21	Added 08-09/2023 field measurements	Yunjia Wu
2023-10-10	Major revision	Yunjia Wu

## Table of Contents

1. Introduction.....	12
2. Sites description.....	13
2.1 SHB site .....	14
2.2 CBM site .....	14
3. Field measurements .....	15
3.1 Field measurement systems .....	15
3.2 Field plots and vertical measurement .....	20
4. Data processing.....	27
5. Results.....	29
5.1 The SHB site .....	29
5.2 The CBM site.....	38
6. Quality assurance.....	45
7. Data access and citation.....	46
7.1 Data access.....	46
7.2 Citation.....	46
References.....	47

## List of Figures

Fig. 1. Location of the SHB (42.6°N,117.3°E) and CBM (42.4°N, 128.1°E) sites in Northern China. The base map is from the ESRI imagery ([https://server.arcgisonline.com/ArcGIS/rest/services/World\\_Imagery/MapServer](https://server.arcgisonline.com/ArcGIS/rest/services/World_Imagery/MapServer)).  
..... 14

Fig. 2. The flux tower + Nikon DHP camera sampling strategy. (a), A flux tower (42.4°N, 117.3°E) at the SHB site; (b), Upward DHP measurement; (c), Platform height measurement. .... 16

Fig. 3. Diagram of the extensible measurement mast with a Nikon fisheye camera fixed on the top. .... 17

Fig. 4. A Nikon D5100 equipped with a Sigma F2.8 EX DC circular fisheye lens. An ultraviolet filter is used to protect the lens from dust or rain. .... 17

Fig. 5. The tower crane + DHP camera sampling strategy. (a), The tower crane with telescopic boom and hook; (b), The crane hook with NIKON DHP camera and micro fisheye camera..... 18

Fig. 6. A UAV with a GoPro DHP camera on top. .... 19

Fig. 7. A GoPro camera with a fisheye lens. .... 19

Fig. 8. The sample plots in the Saihanba site (UTM/50N projection). (a), DNF; (b), DBF; (c), ENF; (d), plot overview; (e), DNF; (f), sample plots in 08/2023. The base map is from ESRI imagery. ([https://server.arcgisonline.com/ArcGIS/rest/services/World\\_Imagery/MapServer](https://server.arcgisonline.com/ArcGIS/rest/services/World_Imagery/MapServer))..21

Fig. 9. (a) The sampling strategy within a plot with five vertical sampling points (VSPs) located at the center and four cardinal points, respectively; (b) A diagram of the portable measurement system; (c) field pictures taken on September 9, 2020, with the upward DHP in the red circle; (d) sample photos at different heights.....23

Fig. 10. Location of the measurement plots, the flux tower and the tower crane at the CBM site. The background image is from Google Earth (October 2017) .....25

Fig. 11. The flux tower (a) and tower crane (b) at the SHB site.....	25
Fig. 12. A classification example in CAN_EYE at Plot A of the SHB site (a) and at the tower crane plot of the CBM site (b). Green and blue colors indicate the foliage and the background sky, respectively. The undesired dark parts are masked out. ....	28
Fig. 13. The vertical profiles of canopy gap fraction at DNF plots A-W on different dates. Plots L and M have no data in September 2022. ....	29
Fig. 14. The vertical profiles of canopy gap fraction at the flux tower plot in different dates (a), and at DNF plots 2B-2L in September 2021 (b).....	30
Fig. 15 The vertical profiles of canopy gap fraction at the DBF and ENF plots in September 2020 and at S1, S2, and S3 plots (DNF) in April 2023.....	30
Fig. 16 The vertical profiles of canopy gap fraction measured in August 2023.....	31
Fig. 17 The vertical profiles of the effective PAI at DNF plots A - W in different dates. Plots L and M have no data in September 2022.....	32
Fig. 18 The vertical profiles of the effective PAI at the flux tower plot in different dates (a), and at DNF plots 2B-2L in September 2021 (b).....	33
Fig. 19 The vertical profiles of the effective PAI at the DBF plots and ENF plots in September, 2020 and at S1, S2, and S3 plots (DNF) in April 2023.....	33
Fig. 20 The vertical profiles of the effective PAI measured in August 2023.....	34
Fig. 21 The vertical profiles of CI at DNF plots A - W in different dates. Plots L and M have no data in September 2022.....	35
Fig. 22 The vertical profiles of CI at the flux tower plot in different dates (a), and at DNF plots 2B-2L in September 2021 (b). ....	36
Fig. 23 The vertical profiles of CI at the DBF and ENF plots in September, 2020 at S1, S2, and S3 plots (DNF) in April, 2023.....	36
Fig. 24 The vertical profiles of canopy gap fraction measured in August 2023.....	37
Fig. 25 The vertical profiles of canopy gap fraction (a), effective PAI (b), and CI (c) at plots A-G in September 2020. ....	38

Fig. 26 The mean directional gap fraction obtained from CAN_EYE at different zenith angles and canopy heights for the flux tower (left) and tower crane (right) plots in September 2022. The horizontal bars show the one standard deviation range. ....	39
Fig. 27 The vertical profiles of $PAI_{eff}$ at the flux tower and tower crane plots in September 2022. ....	40
Fig. 28 The vertical profiles of CI at the flux tower and tower crane plots in September 2022..	40
Fig. 29 UAV photo of the measurement site (a), and vertical profiles of gap fraction (b), effective PAI (c), CI (d) in May 2023.....	41
Fig. 30 The vertical profiles of gap fraction at the tower crane and AA plots in September 2023. ....	42
Fig. 31 The vertical profiles of effective PAI at the tower crane and AA plots in September 2023.....	43
Fig. 32 The vertical profiles of CI at the tower crane and AA plots in September, 2023. ....	43

## List of Tables

Table 1. The SHB measurement records. n is the number of plots. (N: Nikon DHP only; EN: Extensible measurement mast + Nikon DHP; UG: UAV + GoPro DHP; FN: Flux tower + Nikon DHP; ↑: Fixed photo azimuth, with the top pointing north). .....	22
Table 2. The sampling height at the Saihanba flux tower plot (platform heights were manually measured in September 2020).....	23
Table 3. The CBM measurement records. n is the number of plots. There are 16 sampling points around the tower crane (50 m radius) (EN: Extensible measurement mast + Nikon DHP; UG: UAV + GoPro DHP; FN: Flux tower + Nikon DHP; TG: Tower crane + GoPro DHP; TN: Tower crane + Nikon DHP; ↑ : Fixed photo azimuth, with the top pointing north). .....	24
Table 4. Information on the flux tower, tower crane, and other plots in the CBM site. ....	26

## List of Acronyms and Abbreviations

ALA	Average leaf angle
CI	Clumping index
DHP	Digital hemispheric photography
DNF	Deciduous needle forest
DBF	Deciduous broadleaf forest
ENF	Evergreen needle forest
CC	Canopy cover
GEDI	Global Ecosystem Dynamics Investigation
LAI	Leaf area index
LAD	Leaf angle distribution
LUT	Lookup table
MF	Mixed forest
PAI	Plant area index
PAI <sub>eff</sub>	Effective plant area index
SZA	Solar zenith angle
UAV	Uncrewed aerial vehicle
VSP	Vertical sampling points

## 1. Introduction

Leaf area index (LAI), clumping index (CI), and canopy cover (CC) are critical vegetation structural parameters. LAI is defined as one-half of the total green leaf area per unit of ground surface area (Chen and Black, 1992a). CI is the measurement of the spatial distribution pattern of foliage (Chen and Black, 1992b; Nilson, 1971). CC is the fraction of canopy elements vertically projected onto the unit ground surface (Gonsamo et al., 2013; Jennings et al., 1999). LAI, CI, and CC are important in studies of water interception, photosynthesis, and ecosystem dynamics (Gastellu-Etchegorry et al., 1996; Shugart et al., 2010; Simioni et al., 2016). These parameters are related to gap fraction ( $P(\theta)$ ) and can be estimated based on passive remote sensing reflectances. LAI is related to  $P(\theta)$  follows the principles of the Beer-Lambert law, and its retrieval mainly relies on physical or statistical methods (Fang et al., 2019). For example, a global LAI product is derived from VEGETATION reflectances using neural networks over SAIL+PROSPECT radiative transfer model simulations (Baret et al., 2007). Additionally, a long-term global LAI product is generated based on the linear relationship between AVHRR-derived NDVI and MODIS LAI (Liu et al., 2012). CI can be retrieved from gap fraction or size distribution, and global CI products are usually generated based on the linear relationship with the Normalized difference between Hotspot and Darkspot reflectance (Fang, 2021; Pisek et al., 2011; Wei et al., 2019). As for CC, it can be calculated as 1 minus the canopy gap fraction or predicted using reflectance data (Armston et al., 2009; Li et al., 2023). For example, CC is retrieved using Random Forest from Sentinel-2 and Landsat-8 based bands and spectral indices (Bera et al., 2023).

Forest displays a vertical stratification of plant elements, and forest structure can be characterized by the vertical profile of these parameters. The forest structure parameters profile is significant for understanding radiative transfer processes and supporting ecosystem biodiversity evaluation (Bergen et al., 2009; Qi et al., 2019). Lidar is an active remote sensing technology and can map foliage and branch distribution in 3-D space (Lovell et al., 2003; McManamon, 2019). Lidar has shown its advantage for acquiring 3-D canopy structural heterogeneity and revealing vegetation vertical stratification at plot and landscape scales (Detto et al., 2015; Morsdorf et al., 2010). Forest vertical structure parameters are usually derived from lidar data acquired by terrestrial laser scanning (TLS), airborne laser scanning (ALS), and spaceborne laser scanning (SLS) (Tang et al., 2014; Wang and

Fang, 2020; Zheng et al., 2017). Recently, GEDI (Global Ecosystem Dynamics Investigation), launched in 2018, a full waveform spaceborne lidar has provided canopy cover (CC) and plant area index (PAI) vertical profile products in 5 m vertical resolution (Dubayah et al., 2020; Tang and Armston, 2019).

The overall forest structural parameter is typically validated through in-situ measurements conducted using digital cover/hemispherical photography (DHP/DCP), LAI-2200, and TRAC (Dutta et al., 2017; Fang et al., 2018; Ma et al., 2018). The forest vertical structure retrieved from lidar datasets is mainly validated by tower-based measurements (Parker et al., 2001; Tang et al., 2012). However, reference profile measurements can only be obtained from a few towers in the validation sites. Meanwhile, the vertical profile validation is restricted by the orientation and height of the measurement tower. It is necessary to measure the forest structure at different heights to acquire consistent reference data for validation of the vertical canopy structure profile.

Forest structural parameter measurements were implemented by different methods to obtain forest vertical structural data in northern Chian forest sites. A series of DHP measurements were conducted at different forest heights during the leaf-off and leaf-on seasons from 2020 to 2023. This report describes the measurement methods and the resultant forest structure characteristics.

## 2. Sites description

The forest vertical structural measurement was conducted at Saihanba (SHB) National Forest Park (42.6°N, 117.3°E) and Changbai Mountain (CBM) National Nature Reserve (42.4°N, 128.1°E), North China (Fig. 1). The SHB site belongs to the Saihanba National Forest Park (SNFP), widely covered with plantation forest. The CBM site is mainly distributed with primary forest.

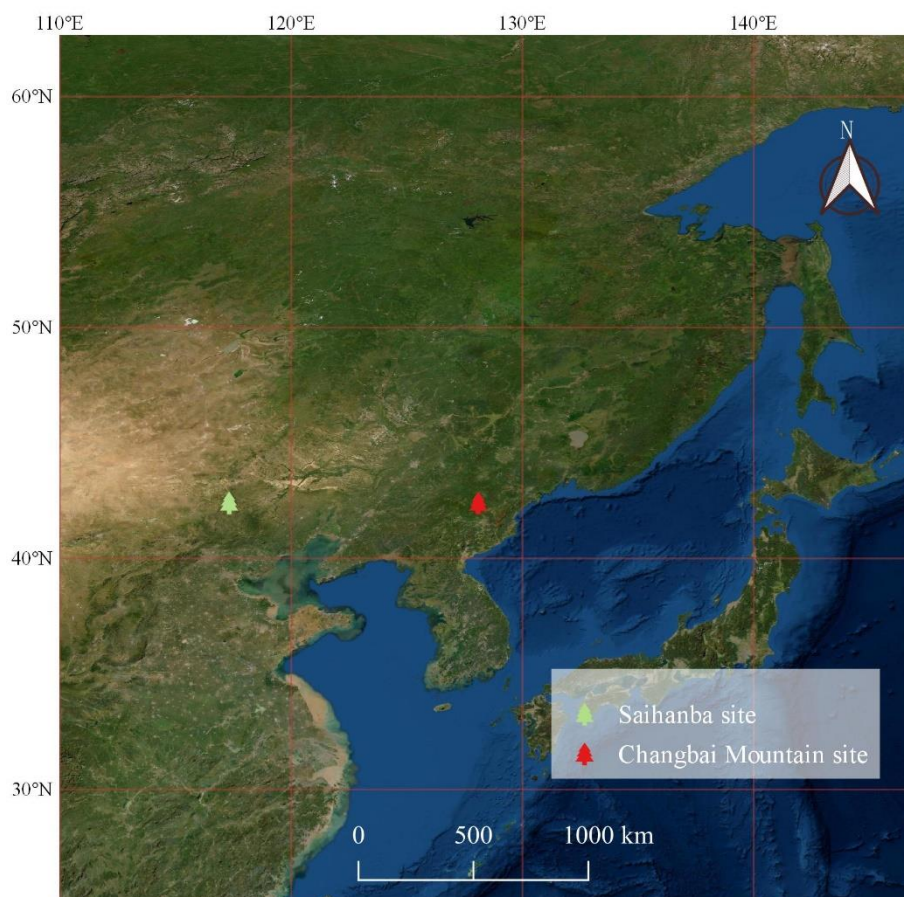


Fig. 1. Location of the SHB (42.6°N,117.3°E) and CBM (42.4°N, 128.1°E) sites in Northern China. The base map is from the ESRI imagery ([https://server.arcgisonline.com/ArcGIS/rest/services/World\\_Imagery/MapServer](https://server.arcgisonline.com/ArcGIS/rest/services/World_Imagery/MapServer)).

## 2.1 SHB site

The SHB experimental site is located in the Hebei Province in North China, within the temperate continental monsoon climate zone. The mean altitude reaches 1700 m above sea level. This region is characterized by a prolonged and cold winter, with an annual mean temperature of  $-1.4\text{ }^{\circ}\text{C}$  and an annual precipitation of 450 mm. The dominant tree species are Mongolian scotch pine (*Pinus sylvestris var-mongolica*), Dahurian larch (*Larix principis-rupprechtii*), and White birch (*Betula platyphylla*). The average tree height is 14.1 m and the tree density is 3500–4000 per ha (Zeng and Wang, 2015).

## 2.2 CBM site

The CBM site is managed by the Research Station of Changbai Mountain Forest Ecosystems, Chinese Academy of Sciences. It is located in the Changbai Mountain National Nature Reserve in the Jilin Province, NE China. The site falls within the temperate continental montane climate zone,

characterized by a prolonged cold winter and a short cool-warm summer. The annual mean temperature ranges between  $-7\text{ }^{\circ}\text{C}$  and  $3\text{ }^{\circ}\text{C}$ . The annual mean precipitation exceeds 600 mm primarily concentrating between June and September. This site is very flat and its altitude ranges from 777 m to 778 m. This relatively homogeneous site is covered with mixed coniferous and broad-leaved trees (Bai et al. 2011). The maximum tree height reaches approximately 30 m.

### **3. Field measurements**

#### **3.1 Field measurement systems**

Four different measurement systems were used considering the actual measurement requirements and equipment optimization (Tables 1 & 2). Almost all measurements were conducted near sunset or under overcast conditions to avoid overexposing of canopy areas or reflections due to direct illuminations (Brüllhardt et al., 2020; Garrigues et al., 2008).

##### **3.1.1 Flux tower + Nikon DHP camera**

In the tower-based measurement (Fig. 2a), a Nikon DHP camera (Fig. 4) mounted on an extendable pole was used to take upward-looking photos. The camera was placed about 1 m from the platform's edge, and images were taken at different available directions of the platform (Fig. 2b). A meter was used for height measurement (Fig. 2c).

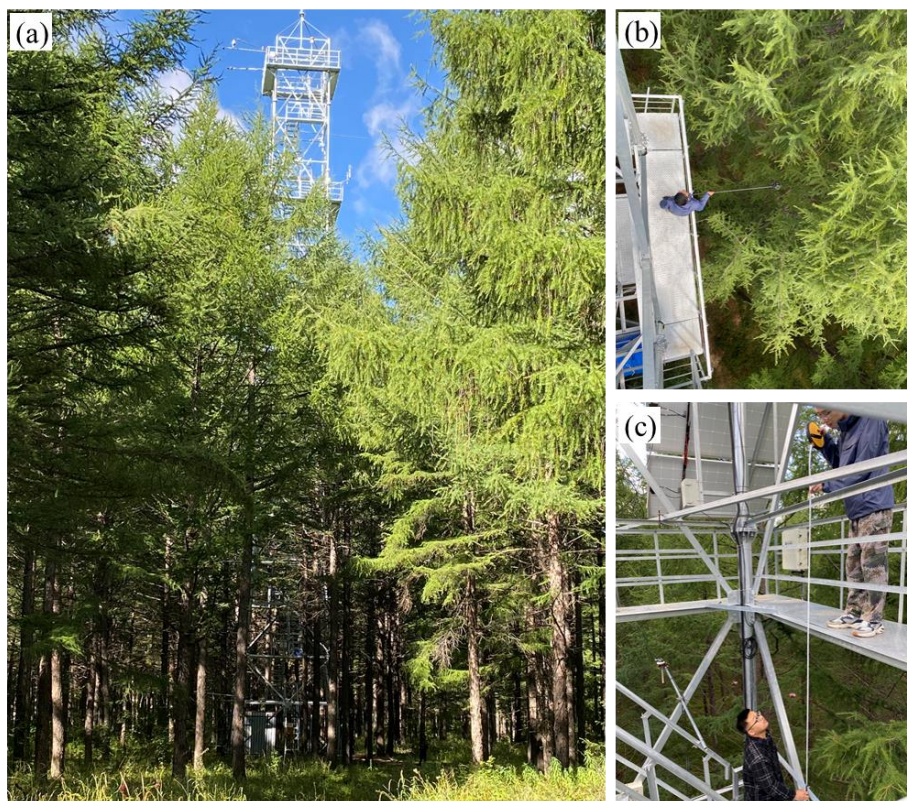


Fig. 2. The flux tower + Nikon DHP camera sampling strategy. (a), A flux tower (42.4°N, 117.3°E) at the SHB site; (b), Upward DHP measurement; (c), Platform height measurement.

### 3.1.2 Extensible measurement mast + Nikon DHP camera

A DHP camera was attached to the top of an extensible mast to take measurements at different heights (Fig. 3). The mast can be extended to a maximum height of 13.5 m. The DHP images were taken using a Nikon D5100 camera and a 4.5 mm F2.8 EX DC circular fisheye convertor (Fig. 4). An ultraviolet cap was used to prevent dust or rain from the lens. System calibration for the DHP camera was performed before measurement according to the CAN\_EYE manual (version 6.4.95), to get the optical center and projection function of the lens (Weiss and Baret, 2010). All photos were stored in high-quality JPEG format at a resolution of 3264×4928. The camera is controlled by a Bluetooth shutter.

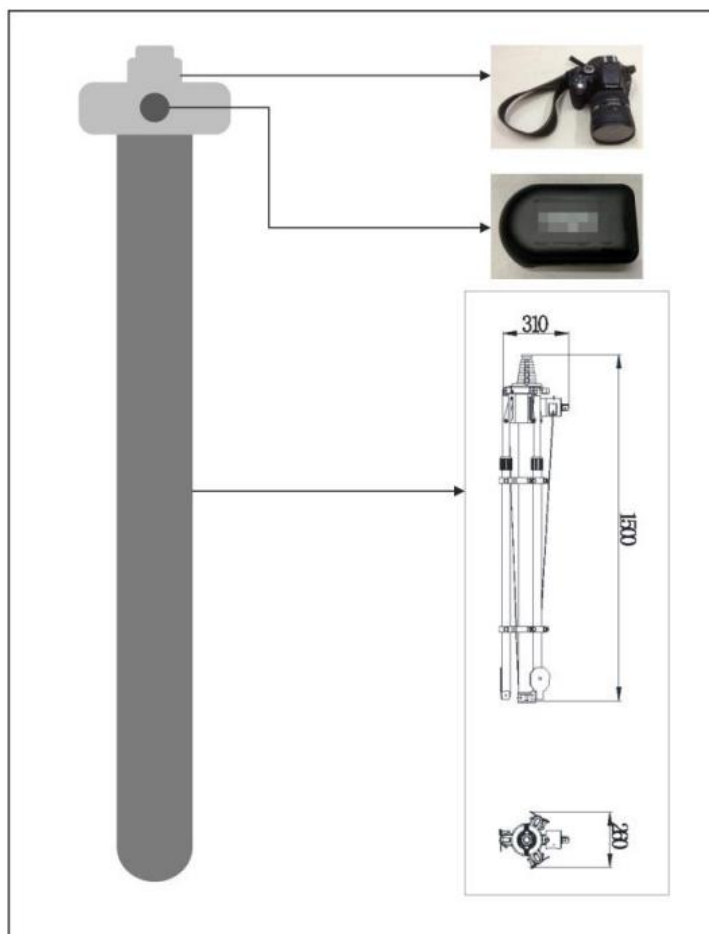


Fig. 3. Diagram of the extensible measurement mast with a Nikon fisheye camera fixed on the top.



Fig. 4. A Nikon D5100 equipped with a Sigma F2.8 EX DC circular fisheye lens. An ultraviolet filter is used to protect the lens from dust or rain.

### 3.1.3 Tower crane + DHP camera

The tower crane has a telescopic boom and can take measurements at various locations and heights (Fig. 6(a)). A Nikon DHP camera and a GoPro DHP camera were fixed at each side of a horizontal monopod (Fig. 6 (b)). The horizontal monopod was fixed to the crane hook. A meter was attached to the monopod for height measurements. Two bubble levels were attached to the camera to maintain their horizontal alignment when taking upward observations.



Fig. 5. The tower crane + DHP camera sampling strategy. (a), The tower crane with telescopic boom and hook; (b), The crane hook with NIKON DHP camera and micro fisheye camera

### 3.1.4 UAV + GoPro DHP camera

A GoPro DHP camera was installed on a UAV to measure different heights through canopy gaps. The height was determined by the built-in GPS positioning system of the UAV (Fig. 6). The GoPro DHP camera is attached with a 180-degree fisheye lens (Fig. 7). The assembled camera is 4.2 cm in height and about 182 g in weight. System calibration was performed for the DHP before measurement according to the CAN\_EYE manual (version 6.4.95) to get the optical center and projection function of the lens (Weiss and Baret, 2010). The optical axis remains in the zenith direction during the

measurement. All photos were stored in high-quality JPEG format at a resolution of 3888× 5184. The camera is controlled by a Bluetooth shutter.



Fig. 6. A UAV with a GoPro DHP camera on top.



Fig. 7. A GoPro camera with a fisheye lens.

## 3.2 Field plots and vertical measurement

### 3.2.1 The SHB site

Totally 59 plots were selected in the SHB site, of which 40 plots are deciduous needle forest (*Larix*), 7 plots are deciduous broadleaf forest plots (*Birch*), 8 plots are evergreen needle forest plots (*Mongolian scotch pine*), and 4 plots are mixed forest (Fig. 8). Contiguous measurements were conducted at most plots (except TLS and Flux tower plots) located at the GEDI V2 footprints (Table 1). A flux tower (Fig. 8a) was built by the State Key Laboratory of Remote Sensing Science, Jointly Sponsored by the Aerospace Information Research Institute, Chinese Academy of Sciences and Beijing Normal University. The tower is 45 m height and measurements were made at the tower platforms at different heights.

The DHP sample is located within a 15 m radius area around the GEDI footprints at most plots in the SHB site (Fig. 9). Five vertical sampling points (VSPs) are located at the center and four cardinal points. At each VSP, a brick was used as a marker to designate the location for consecutive measurements (Fig. 9a). The sampling time and strategy at each plot are shown in Table 1. The *extensible measurement mast + Nikon DHP camera strategy* was used in the measurement from 2020 to 2022. The upward DHP observation was made close to the ground, and from 1.5 m to 13.5 m in 2 m intervals (Fig. 9b-c). At each height of each VSP, at least 4 photos were taken by Nikon DHP (Fig. 9d). At the flux tower plot, the DHP was placed about 1 m from the platform's edge to take at least 8 upward photos at different available directions (Table 2). In 2023, the *UAV + GoPro DHP camera sampling strategy* was used to take measurements from 0 m up to the canopy top in 2 m and 5 m intervals. At least 2 photos were taken by GoPro DHP at each height of each VSP. The azimuth of the photos was fixed, with the top pointing north in August 2023 (Table 1).

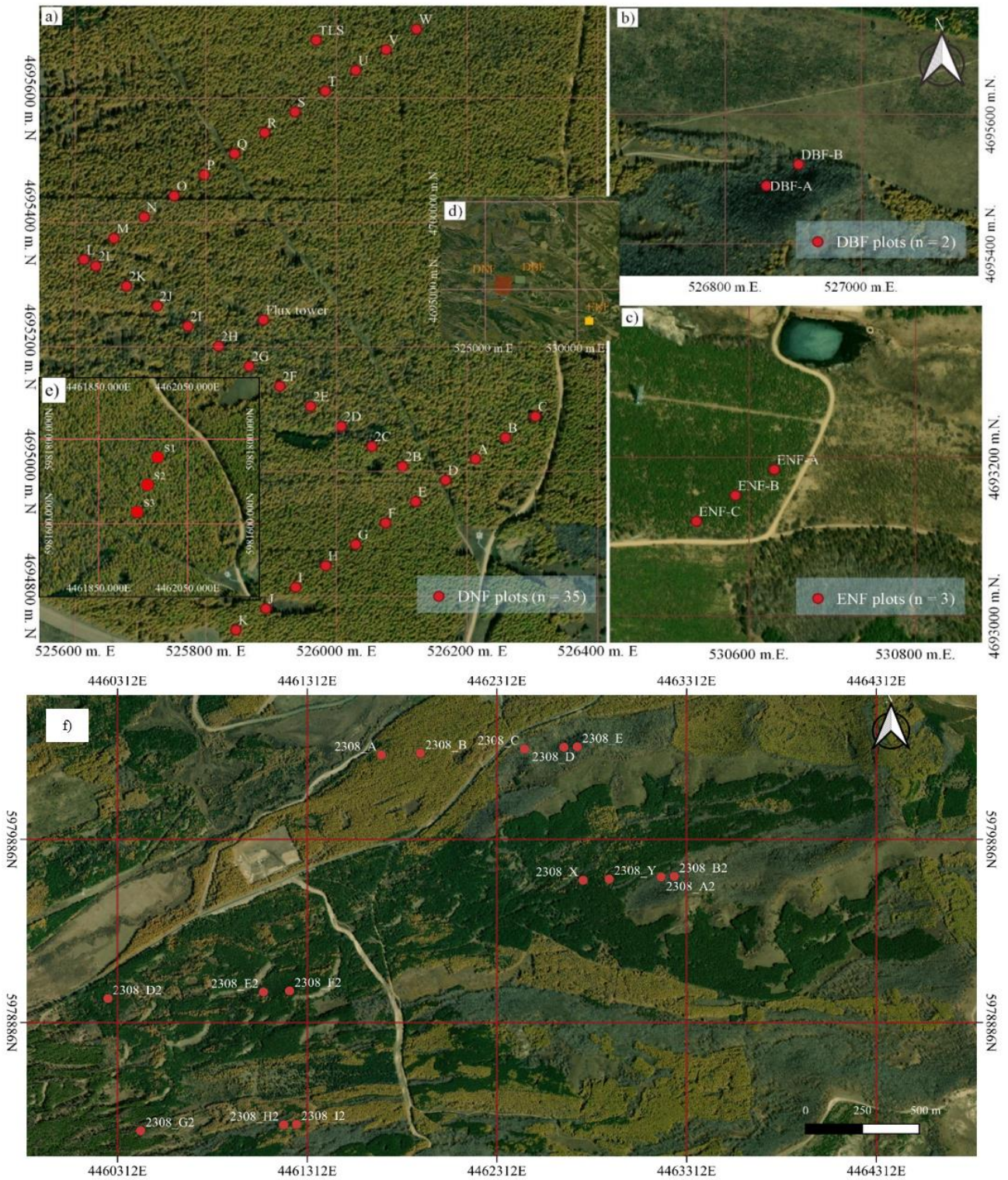


Fig. 8. The sample plots in the Saihanba site (UTM/50N projection). (a), DNF; (b), DBF; (c), ENF; (d), plot overview; (e), DNF; (f), sample plots in 08/2023. The base map is from ESRI imagery. ([https://server.arcgisonline.com/ArcGIS/rest/services/World\\_Imagery/MapServer](https://server.arcgisonline.com/ArcGIS/rest/services/World_Imagery/MapServer))

Table 1. The SHB measurement records. n is the number of plots. (**EN**: Extensible measurement mast + Nikon DHP; **UG**: UAV + GoPro DHP; **FN**: Flux tower + Nikon DHP; **↑**: Fixed photo azimuth, with the top pointing north).

Plots	September, 2020	April, 2021	June, 2021	September, 2021	August, 2022	April, 2023	August, 2023
A-W (DNF, n=23)	<b>EN</b>	<b>EN</b>	<b>EN</b>	<b>EN</b>			
2B-2L (DNF, n=11)				<b>EN</b>			
TLS (DNF)		<b>EN</b>					
Flux tower (DNF)	<b>FN</b>		<b>FN</b>	<b>FN</b>	<b>FN</b>		<b>UG ↑</b>
DBF (A, B)	<b>EN</b>						
ENF (A, B, C)	<b>EN</b>						
S1-S3 (DNF, n=3)						<b>UG</b>	
2308_A, 2308_G2-I2 (MF, n=4)							<b>UG ↑</b>
2308_B (DNF, n=1)							<b>UG ↑</b>
2308_C-E, 2308_A2- B2(DBF, n=5)							<b>UG ↑</b>
2308_X-Y, 2308_D2-F2 (ENF, n=5)							<b>UG ↑</b>

Table 2. The sampling height at the Saihanba flux tower plot (platform heights were manually measured in September 2020).

Height (m)	Direction
Ground	All directions
3.7 m	West
6.2 m	East
8.7 m	West
11 m	East
13.5 m	West
16 m	All directions
18.5 m	West

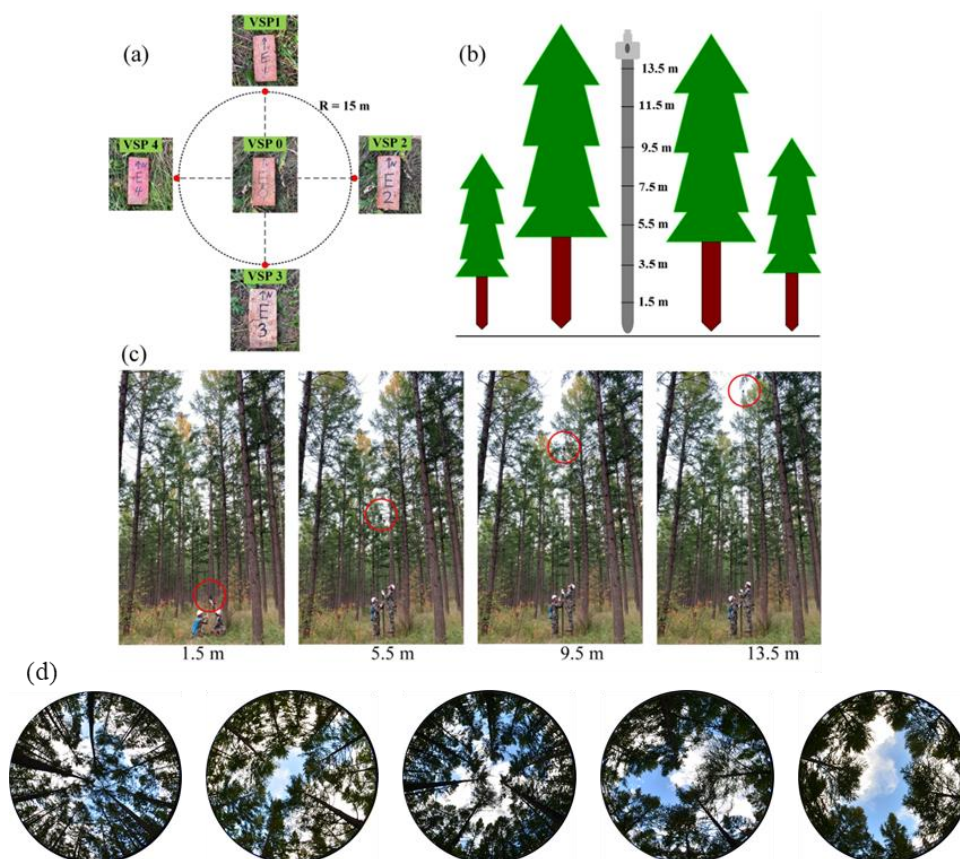


Fig. 9. (a) The sampling strategy within a plot with five vertical sampling points (VSPs) located at the center and four cardinal points, respectively; (b) A diagram of the portable measurement system; (c) field pictures taken on September 9, 2020, with the upward DHP in the red circle; (d) sample photos at different heights.

### 3.2.2 The CBM site

Totally 10 plots were selected in the CBM site in different years (Fig. 10). Most plots (A to G) were located at the GEDI V2 footprints. A flux tower and a tower crane about 100 m apart were constructed on this site for scientific experiments. The flux tower is about 60 m in height and has several platforms at different heights that can be used for measurement (Fig. 11a). The tower crane covers an area of a 50 m radius (Fig. 11b). It runs on electric power and a professional operator moves the crane arm and lifts the hook to different heights. Sixteen evenly distributed points around the crane (Fig. 10) were selected to take upward DHP observations. In September 2023, a new square plot named AA with a side length of 30 m was selected for long-term measurement (Fig. 10).

The sampling strategies and times for these plots are listed in Table 3. The height interval and the number of photos taken at each height for each sampling strategy are listed in Table 4. Note that the measurement starts from 1.5 m height for the *tower crane + DHP camera* measurement strategy. Some measurements were made with the same observation azimuth, i.e., the top facing north (Table 3).

Table 3. The CBM measurement records. n is the number of plots. There are 16 sampling points around the tower crane (50 m radius) (EN: Extensible measurement mast + Nikon DHP; UG: UAV + GoPro DHP; FN: Flux tower + Nikon DHP; TG: Tower crane + GoPro DHP; TN: Tower crane + Nikon DHP; ↑: Fixed photo azimuth, with the top pointing north).

Plot	September, 2020	September, 2022	May, 2023	September, 2023
A-G (n=7)	<b>EN</b>			
Flux tower		<b>FN</b>		
Tower crane		<b>TN</b>	<b>UG TN TG</b>	<b>(UG ↑) TN TG</b>
AA				<b>UG ↑</b>



Fig. 10. Location of the measurement plots, the flux tower and the tower crane at the CBM site. The base map is from the ESRI imagery ([https://server.arcgisonline.com/ArcGIS/rest/services/World\\_Imagery/MapServer](https://server.arcgisonline.com/ArcGIS/rest/services/World_Imagery/MapServer)).



Fig. 11. The flux tower (a) and tower crane (b) at the SHB site.

Table 4. Information on the flux tower, tower crane, and other plots in the CBM site.

Plots	Latitude	Longitude	Atitude	Maximum height	Sampling height	photos/height	Fixed azimuth
Flux tower	42°24'12.21"N	128°05'50.19"E	776.92 m	35 m	0,8,16,22,26 m	> 12 (until 2023)	
Tower crane	42°24'14.37"N	128°05'46.31"E	776.05 m	60 m	0 to 24 m with 2 m interval (until 2022) 0 to 24 m with 2 m and 5 m interval (after 05/2023)	2 <sup>2</sup>	✓(only for UVA + GoPro DHP camera strategy after September 2023)
AA	42°24'14.19"N	128°06'8.69"E	776.00m	/	0 to 22 m with 2 m and 5 m interval (after 08/2023)	2 / VSP	✓
A-G	/	/	/	/	0 to 24 m with 2 m interval, 15.5, 16.5 m (until 2023)	4 / VSP	

## 4. Data processing

All valid photos from each plot were processed by the CAN\_EYE software to obtain the structural parameters (Weiss et al., 2004). The maximum viewing angles were set to 60°. The angular resolutions for both zenith and azimuth directions were set to 2.5°. The classification of foliage from the background was conducted interactively by manually determining sky or foliage pixels in CAN\_EYE. Undesired image parts, such as tower components, were masked out during image processing. Fig. 12 presents an example of the upward DHP classification results for different measurement plots. More detailed processing procedures can be found in the CAN\_EYE manual (Weiss and Baret, 2017).

CAN-EYE calculates the canopy gap fraction from the classified images at different angles. The gap fraction can generally be expressed as an exponential function of the LAI under random turbid medium assumption. A gap fraction ( $P(\theta)$ ) lookup table (LUT) is generated by varying LAI (0–10) and ALA (10°–80°) values based on the Beer-Lambert's law (Nilson, 1971):

$$P(\theta) = e^{-G(\theta) \cdot PAI_{eff} / \cos(\theta)} \quad (1)$$

where  $P(\theta)$  is the canopy gap fraction at direction  $\theta$ , and  $G(\theta)$  is the leaf projection function. The  $P(\theta)$  and the corresponding effective PAI and ALA can be solved based on the minimum cost function value.

The whole  $P$  is calculated as a simple average of the directional  $P(\theta)$ :

$$P = \frac{1}{N} \sum_{i=1}^N P(\theta_i) \quad (2)$$

The clumping index (CI) at direction  $\theta$  is computed using the logarithm gap fraction averaging method (Lang and Yueqin, 1986):

$$CI(\theta) = \frac{\ln \overline{P(\theta)}}{\overline{\ln P(\theta)}} \quad (3)$$

The whole CI (0–60°) is calculated from the directional CI (Stenberg et al., 2014):

$$CI = \int_0^{\pi/2} CI(\theta) \sin \theta d\theta \quad (4)$$

Combining Eqs. (1) and (4), the true PAI and WAI are derived as:

$$PAI = PAI_{eff} / CI \quad (5)$$

In this report, the method V6.1 results were used for further analysis.

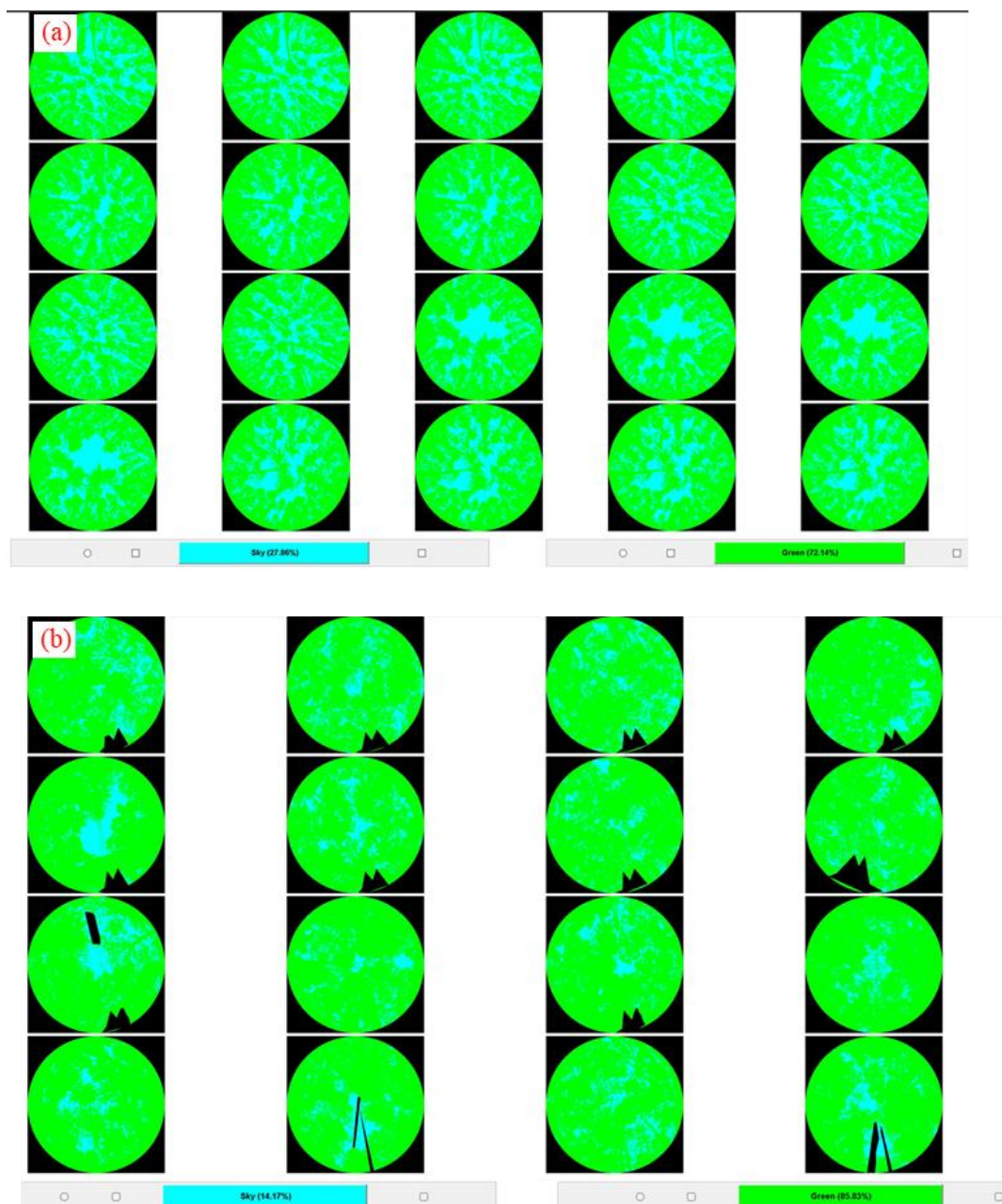


Fig. 12. A classification example in CAN\_EYE at Plot A of the SHB site (a) and at the tower crane plot of the CBM site (b). Green and blue colors indicate the foliage and the background sky, respectively. The undesired dark parts are masked out.

## 5. Results

### 5.1 The SHB site

#### 5.1.1 Gap fraction

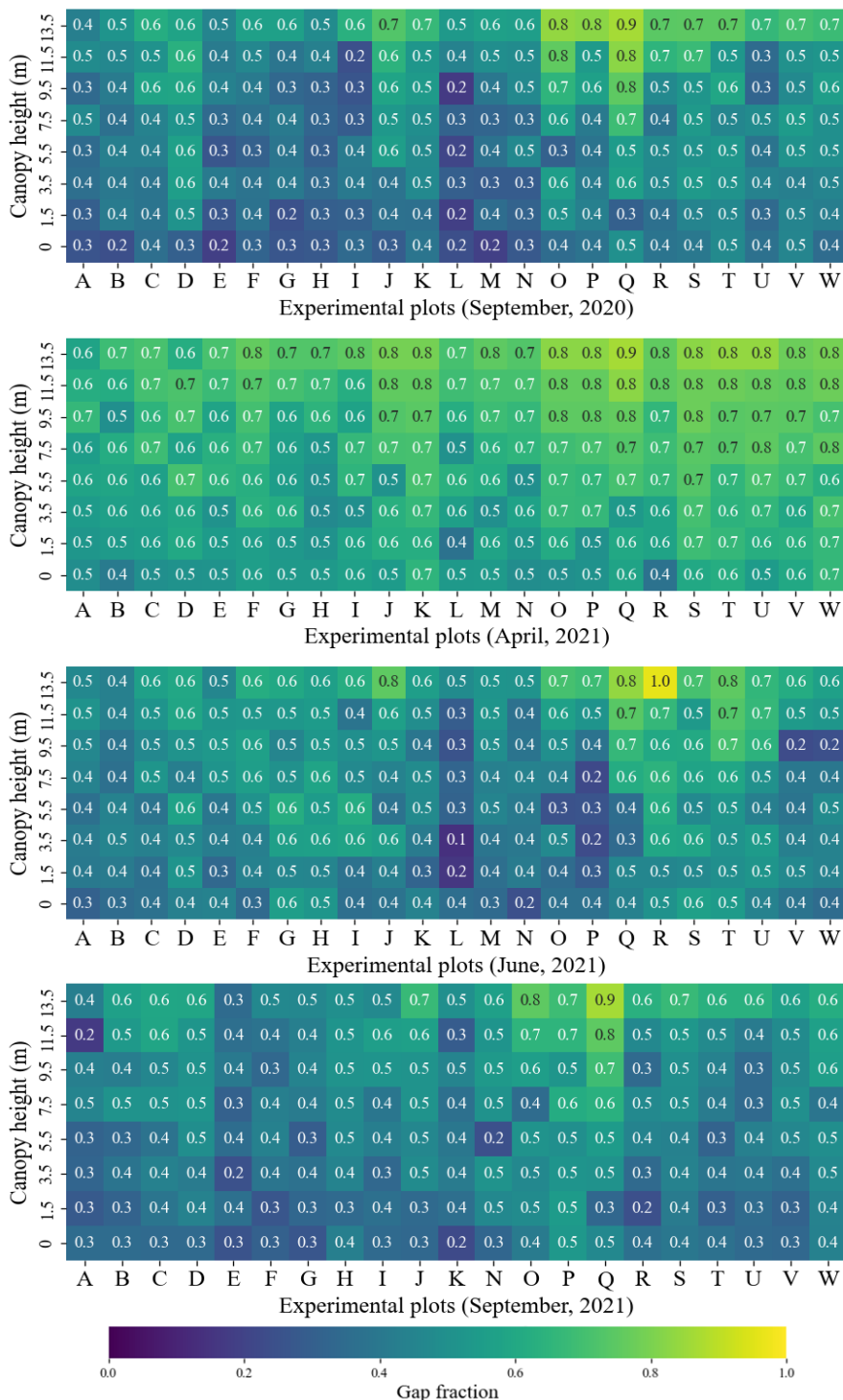


Fig. 13. The vertical profiles of canopy gap fraction at DNF plots A-W on different dates. Plots L and M have no data in September 2022.

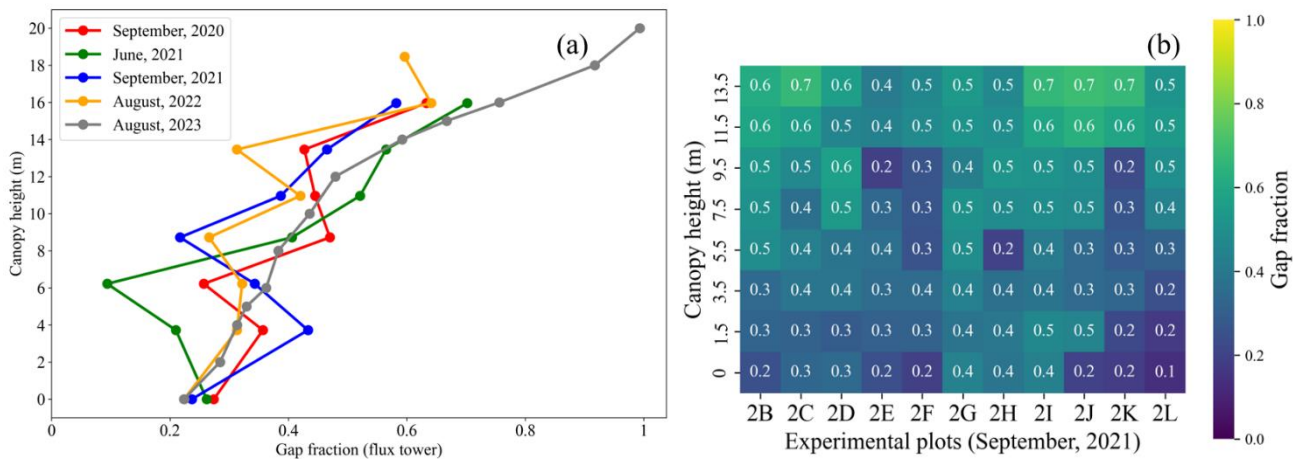


Fig. 14. The vertical profiles of canopy gap fraction at the flux tower plot in different dates (a), and at DNF plots 2B-2L in September 2021 (b).

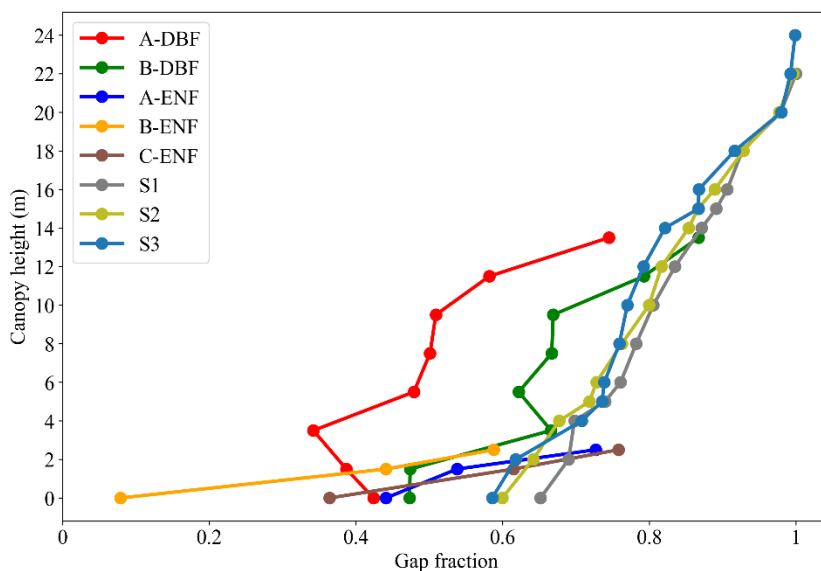


Fig. 15 The vertical profiles of canopy gap fraction at the DBF and ENF plots in September 2020 and at S1, S2, and S3 plots (DNF) in April 2023.

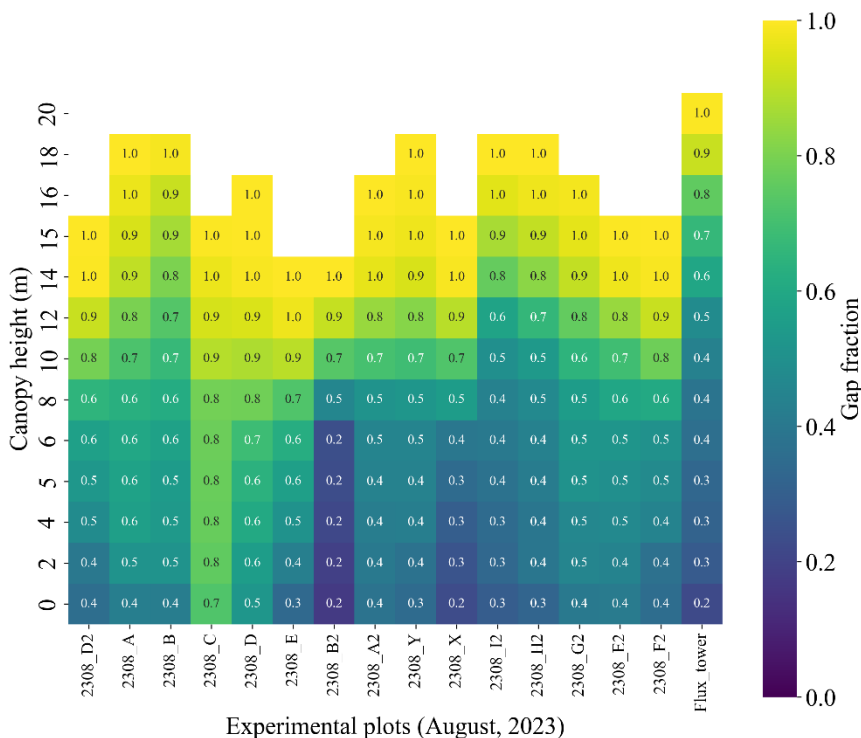


Fig. 16 The vertical profiles of canopy gap fraction measured in August 2023.

Fig. 13 shows the  $P(\theta)$  at plots A-W during the leaf-on and leaf-off seasons. Plots O, Q, and R show relatively larger gap fractions on four dates between 9.5 m and 13.5 m. At the flux tower plot, Fig. 14a shows that the vertical  $P(\theta)$  profile obtained in different measurement dates are consistent. The largest difference between the dates was observed at 6.2 m. Fig. 14b shows the vertical  $P(\theta)$  profile at plots 2B-L. The  $P(\theta)$  distribution at plots 2E, 2F, and 2K displays impractical variation, probably because the measurement is too close to the foliage in the middle of the canopy. Among the DBF and ENF plots, plot B-ENF shows the greatest  $P(\theta)$  variation from 0.07 at the ground to 0.59 at the 2.5 m height (Fig. 15). The  $P(\theta)$  at plots S1, S2, and S3 are highly consistent (leaf-off season, Fig. 15). Fig. 16 shows the  $P(\theta)$  measured in August 2023 (leaf-on season).

### 5.1.2 Effective PAI

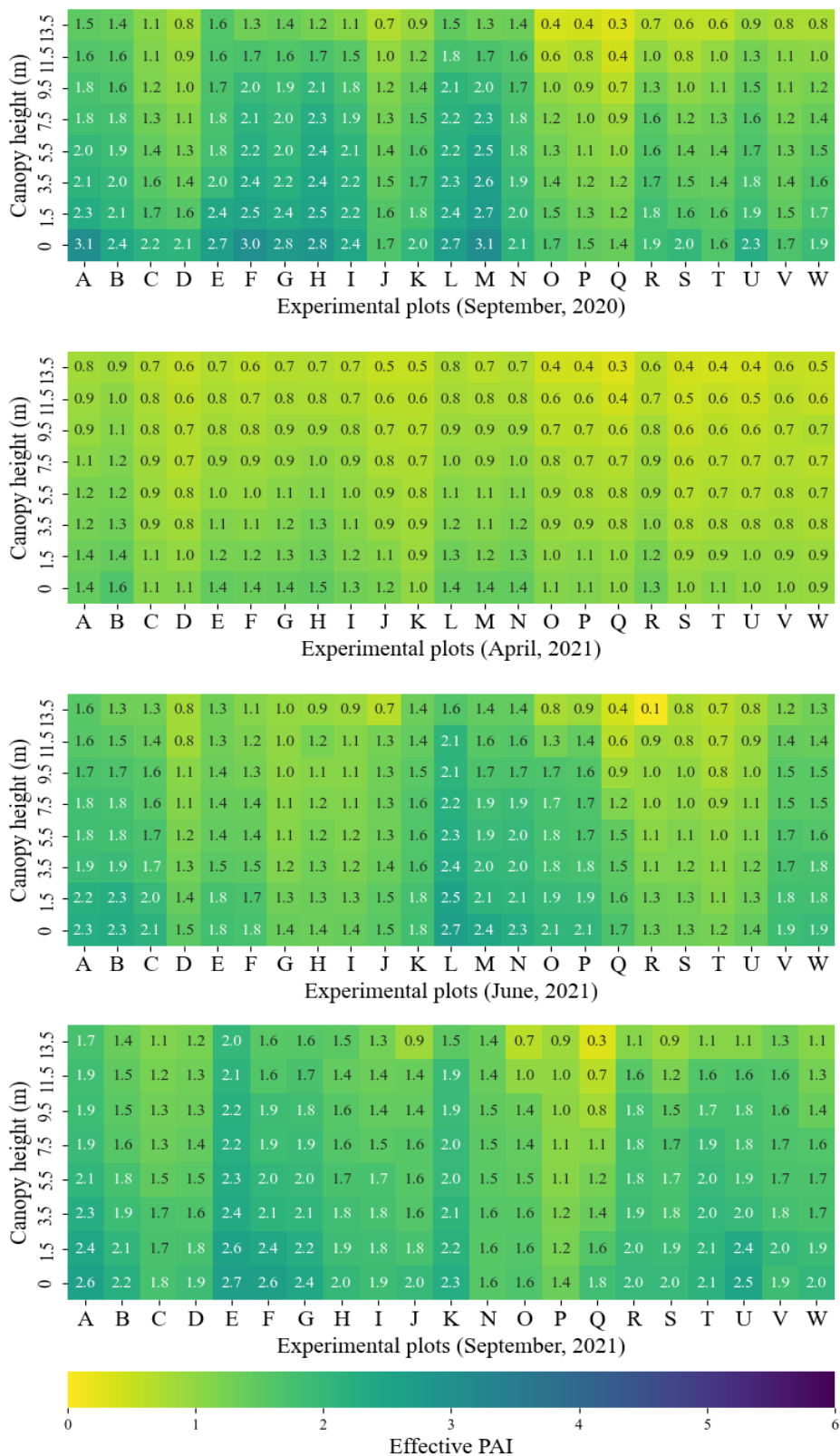


Fig. 17 The vertical profiles of the effective PAI at DNF plots A - W in different dates. Plots L and M have no data in September 2022.

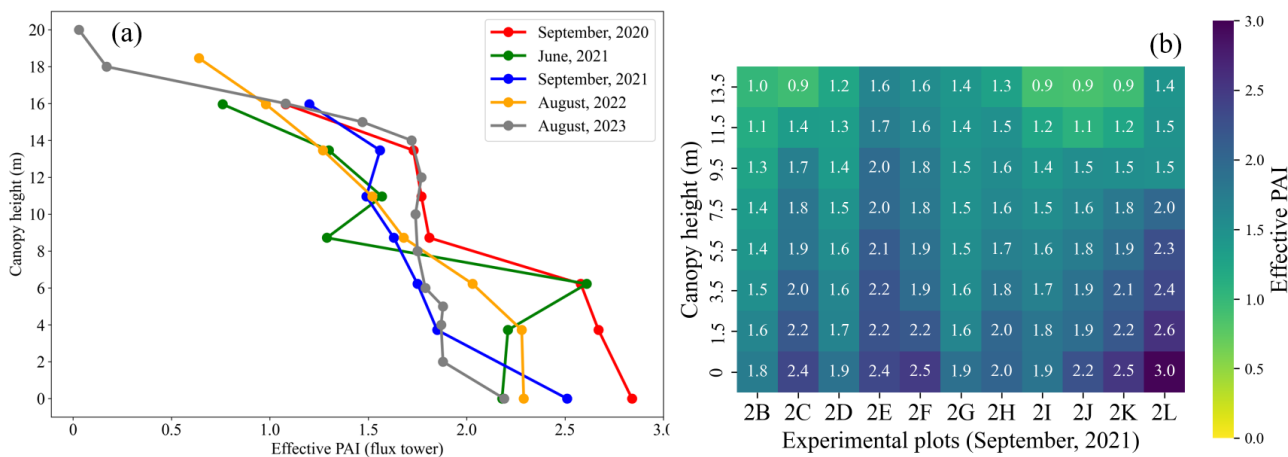


Fig. 18 The vertical profiles of the effective PAI at the flux tower plot in different dates (a), and at DNF plots 2B-2L in September 2021 (b).

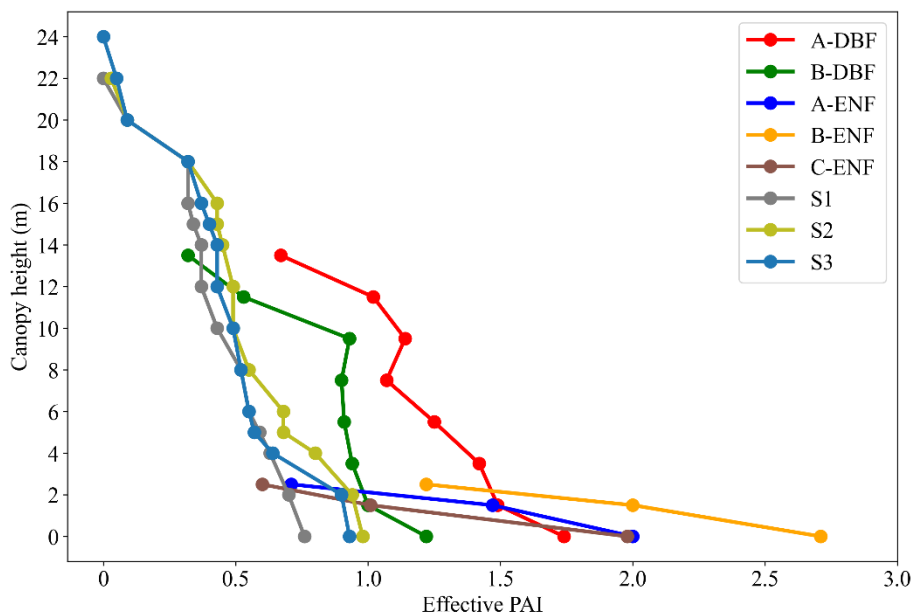


Fig. 19 The vertical profiles of the effective PAI at the DBF plots and ENF plots in September, 2020 and at S1, S2, and S3 plots (DNF) in April 2023.

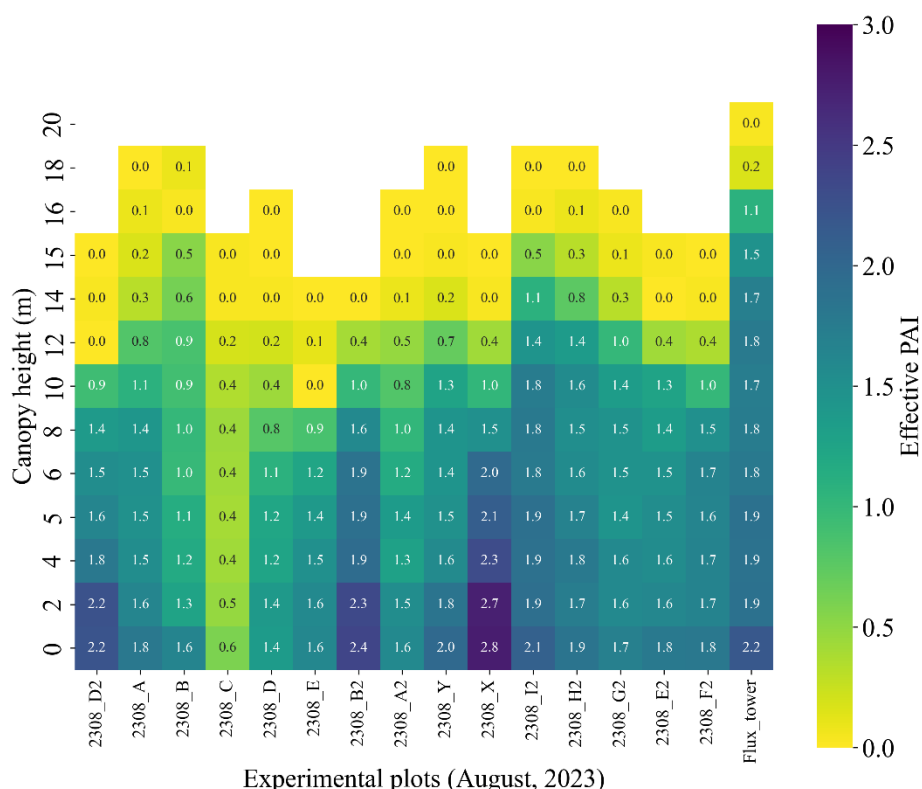


Fig. 20 The vertical profiles of the effective PAI measured in August 2023.

Fig. 17 shows the variation of the effective PAI at different plots on multiple observation dates. Plots A, F, L, and M generally show larger PAI<sub>eff</sub> than those of the other plots in the leaf-on season. The average PAI<sub>eff</sub>(1.68) observed in September 2021 is greater than those in September 2020 (1.61) and June 2021 (1.45). The relatively high PAI<sub>eff</sub> was observed at plots R, S, T, U, V, and W in September 2021 because of forest growth. Fig. 18a shows the vertical PAI<sub>eff</sub> profile derived from different sampling strategies at the flux tower plot. Fig. 18b shows vertical the PAI<sub>eff</sub> profile at plots 2B-2L measured in September 2021. Plots 2C, 2E, 2F, 2K, and 2L display large vertical PAI<sub>eff</sub> profiles compared to other plots. Fig. 19 shows the PAI<sub>eff</sub> measured at the DBF, ENF, and DNF plots, respectively. The largest overall PAI<sub>eff</sub> was observed at plot B-ENF (> 2.5). Fig. 20 shows the vertical PAI<sub>eff</sub> profile measured at heights up to 20 m in August 2023. The overall PAI<sub>eff</sub> varies between 2 and 2.5. PAI<sub>eff</sub> varies greatly from 8 m to 14 m, possibly because leaves are more concentrated at < 10 m (Fig. 20).

### 5.1.3 Clumping index

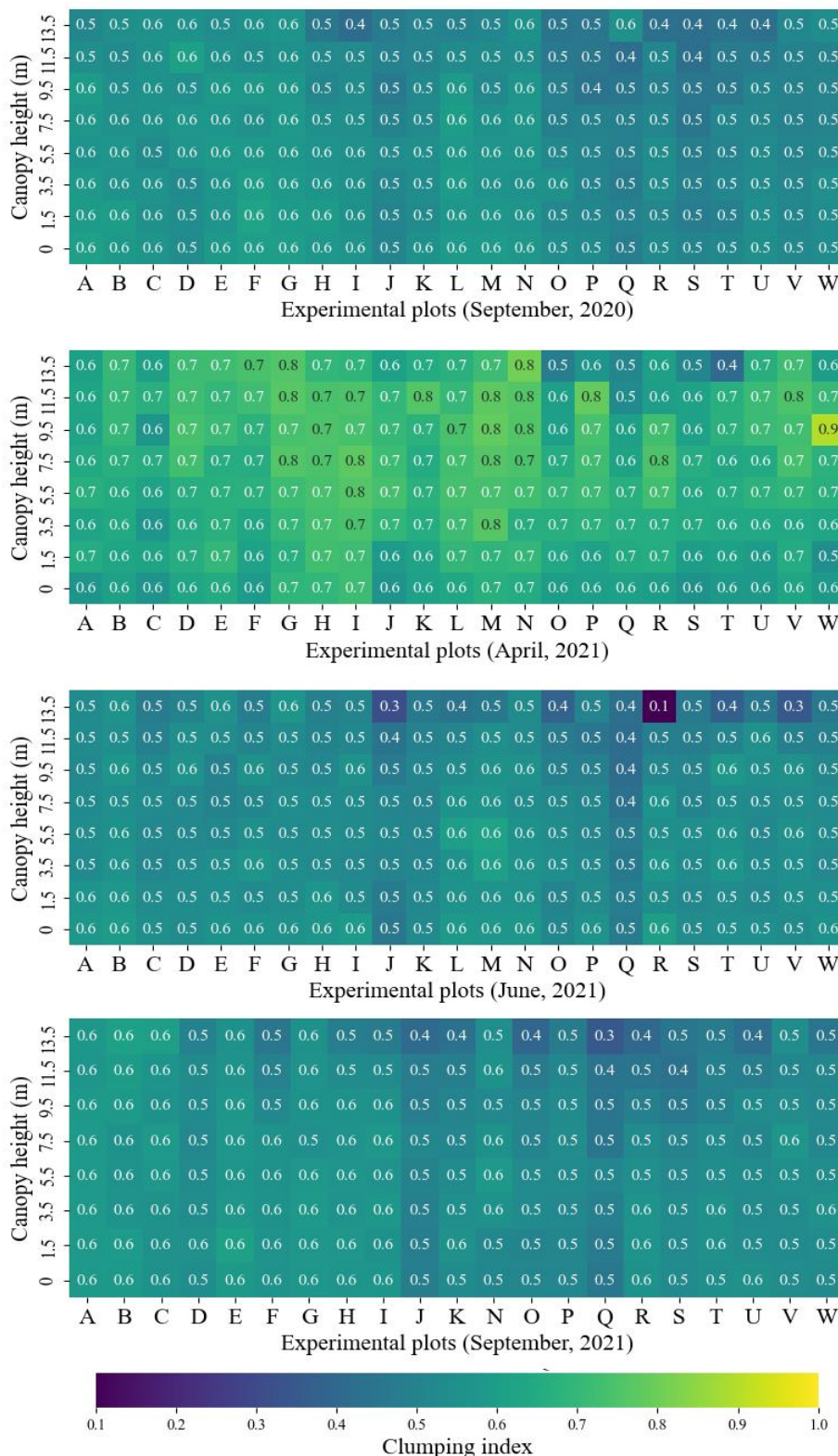


Fig. 21 The vertical profiles of CI at DNF plots A - W in different dates. Plots L and M have no data in September 2022.

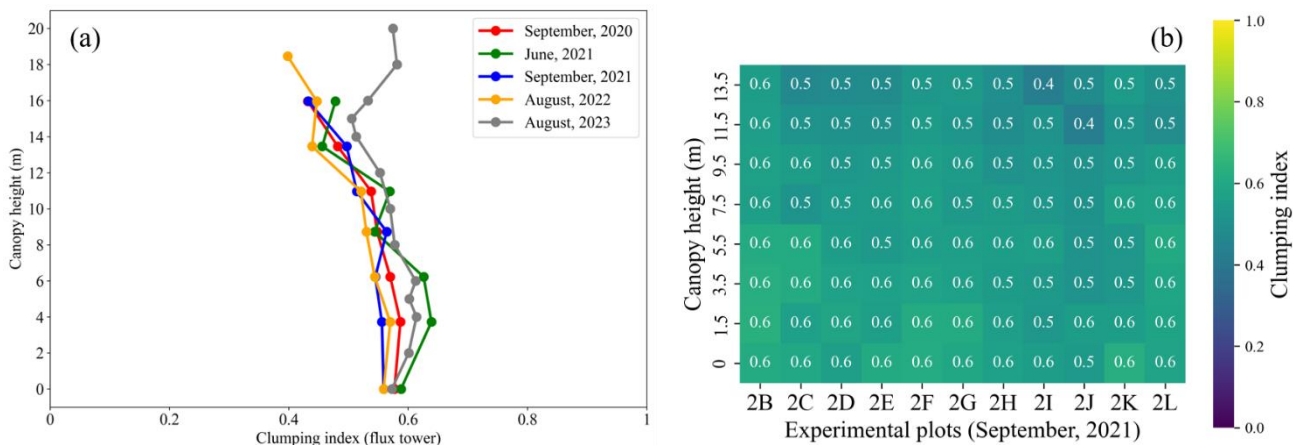


Fig. 22 The vertical profiles of CI at the flux tower plot in different dates (a), and at DNF plots 2B-2L in September 2021 (b).

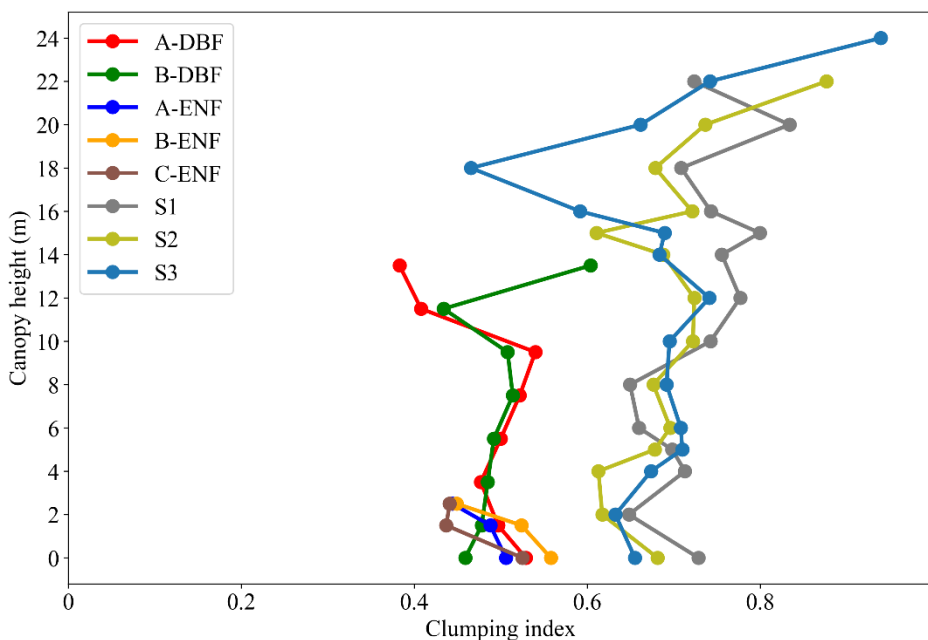


Fig. 23 The vertical profiles of CI at the DBF and ENF plots in September, 2020 at S1, S2, and S3 plots (DNF) in April, 2023.

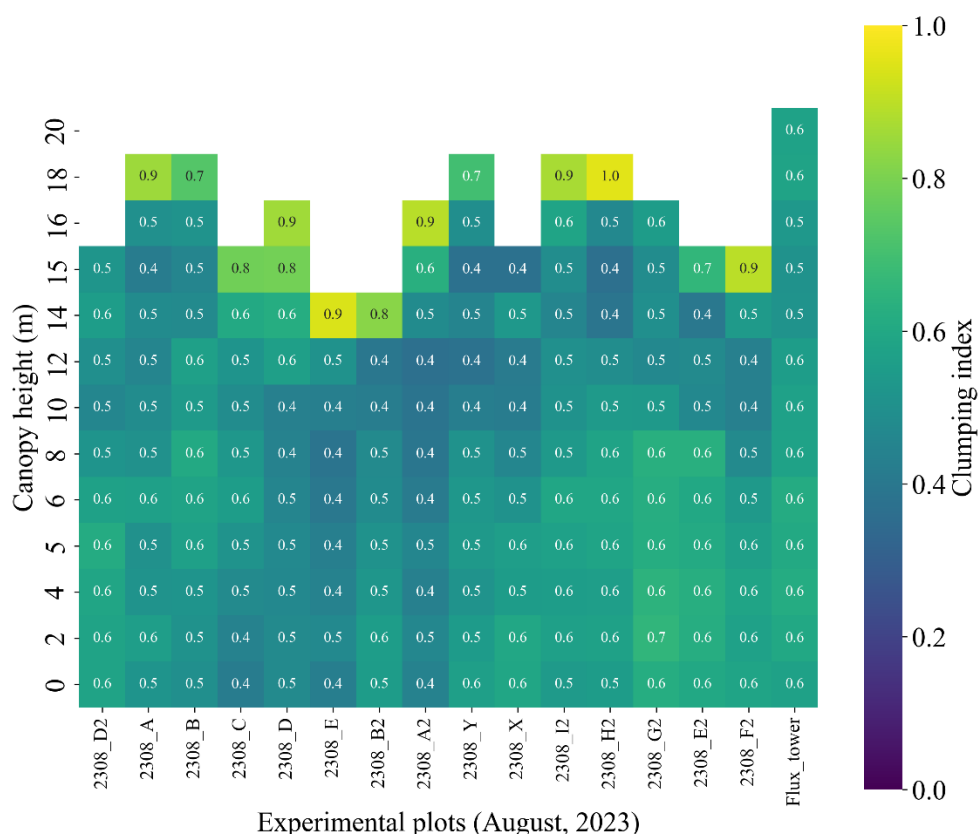


Fig. 24 The vertical profiles of CI measured in August 2023.

The vertical CI profiles are compared between the DNF plots on multiple observation dates (Fig. 21). The average overall CI on all plots is around 0.52 and 0.67 in the leaf-on and leaf-off seasons, respectively. The canopy top CI is relatively small because of the larger  $P(\theta)$  and clumped foliage distribution. The CI at the flux tower (Fig. 22a) is consistent between different dates. The CI ranges from 0.55 to 0.6 at the ground and then slightly decreases with the increase of canopy height (Fig. 22a). At the DNF plots 2B-2L, The vertical CI profile shows similar variation and the average CI at the ground is 0.586 and decreases to about 0.5 at the canopy top (Fig. 22b). The DBF CIs are similar from 3.5 m to 7.5 m (Fig. 23). The CI values measured in April 2023 fluctuated around 0.7 (Fig. 23). In August 2023, the CI was around 0.6 at ground, and gradually decreased with height, but increased again at the canopy top (Fig. 24). Previous measurements before April 2023 did not detect an increasing trend in the canopy top CI, because of the measurement height limit.

## 5.2 The CBM site

### 5.2.1 September 2020

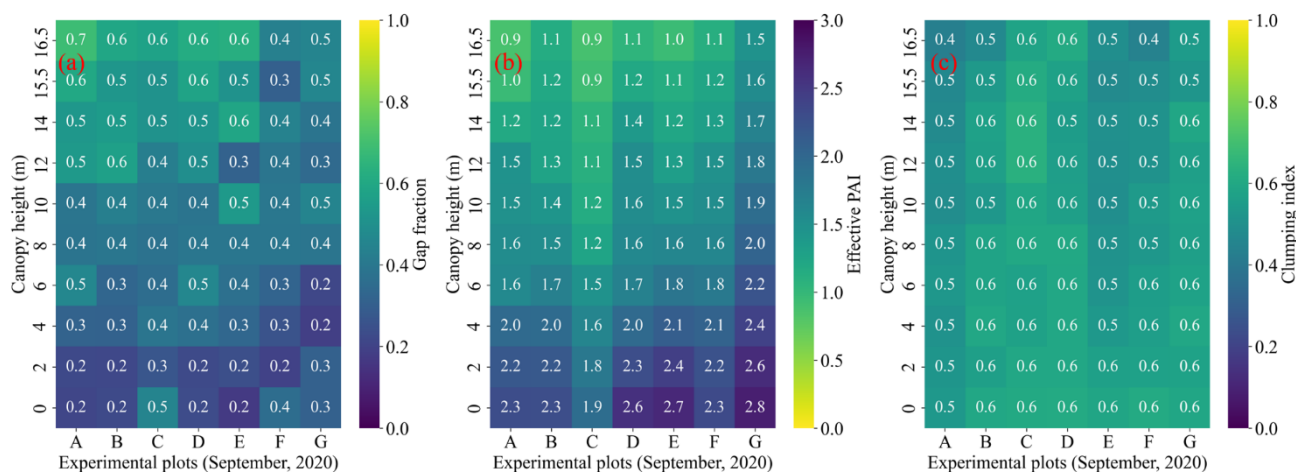


Fig. 25 The vertical profiles of canopy gap fraction (a), effective PAI (b), and CI (c) at plots A-G in September 2020.

The vertical  $P(\theta)$ ,  $PAI_{eff}$ , and CI profile from ground to 16.5 m height at 7 plots are shown in Fig. 25. The extensible mast can reach a maximum of 16.5 m, smaller than the canopy top height.  $P(\theta)$  ranges from 0.2 to 0.7 from ground to 16.5 m.  $PAI_{eff}$  is smaller than 3 and larger than 0.9 in all plots. Relatively larger  $PAI_{eff}$  values are observed in plots D, E, and G. Overall, CI ranges from 0.4 at 16.5 m to 0.6 at the ground. The distinct CI difference between different plot is observed at at height  $> 15.5$  m.  $PAI_{eff}$  displays an overall positive correlation with CI. The  $P(\theta)$  and  $PAI_{eff}$  does not show a rigorous negative correlation. For example, the  $P(\theta)$  below 4 m at plot G is larger than that within 4-6 m but the  $PAI_{eff}$  below 4 m shows a large value.

### 5.2.2 September 2022

#### (1) Zenithal gap fraction

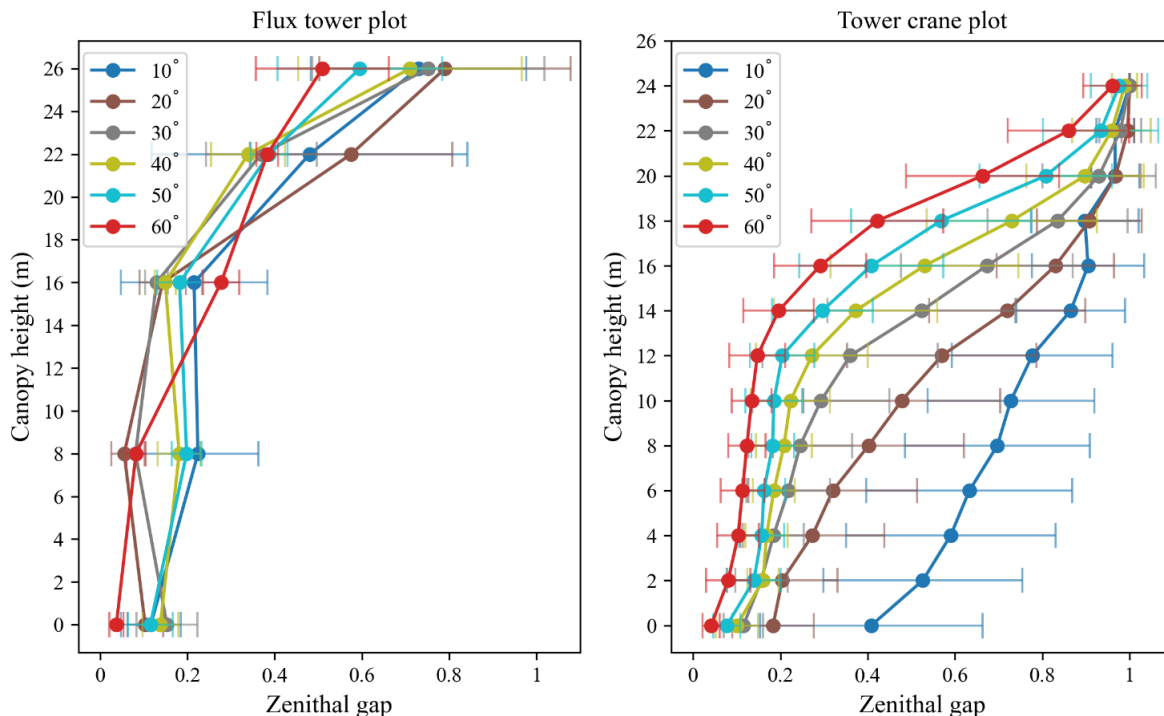


Fig. 26 The mean directional gap fraction obtained from CAN\_EYE at different zenith angles and canopy heights for the flux tower (left) and tower crane (right) plots in September 2022. The horizontal bars show the one standard deviation range.

The directional  $P(\theta)$  were averaged at every  $10^\circ$  zenith angle interval at different heights for the flux tower and tower crane plots (Fig. 26). The  $P(\theta)$  at both plots shows an increasing trend with the height. At the flux tower plot, the gaps show small differences at different zeniths but the standard derivations gradually increase from the ground to the canopy top. On the contrary, at the tower crane plot, the  $P(\theta)$  over  $10^\circ$  zenithal is larger than that over other zeniths at  $<16$  m. The standard deviation decreases from the ground to the canopy top.

#### (2) Effective PAI

Fig. 27 shows the effective PAI for the flux tower and the tower crane plots. The overall  $PAI_{eff}$  for the two plots are 3.68 and 4.08, respectively. At the tower crane plot, the  $PAI_{eff}$  decreases by 1.04 from the ground to 4 m then decreases slowly from 2.64 to 1.94 from 4 m to 14 m. The measurement

interval is larger at the flux tower plot. The  $PAI_{eff}$  at the flux tower plot is close to 1.0 at height > 22 m.

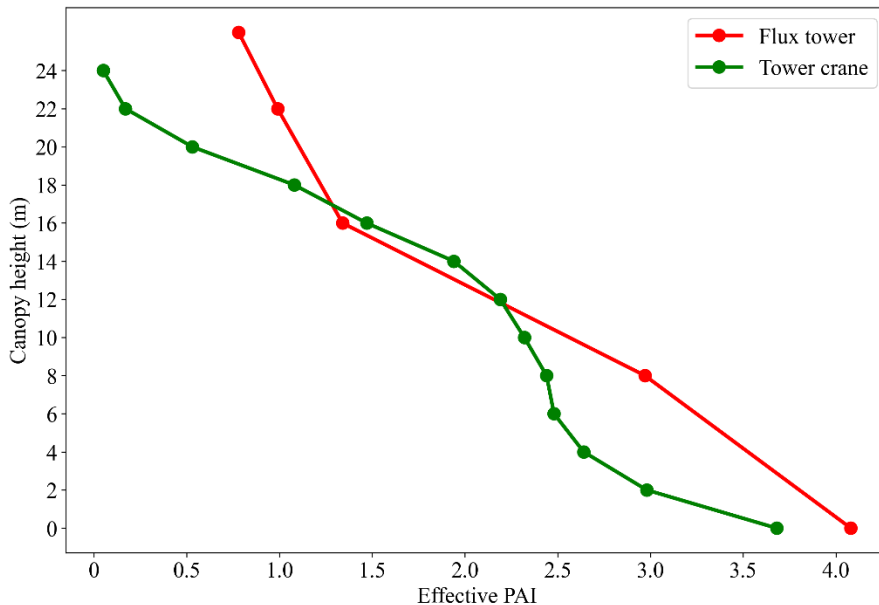


Fig. 27 The vertical profiles of  $PAI_{eff}$  at the flux tower and tower crane plots in September 2022.

**(3) Clumping index**

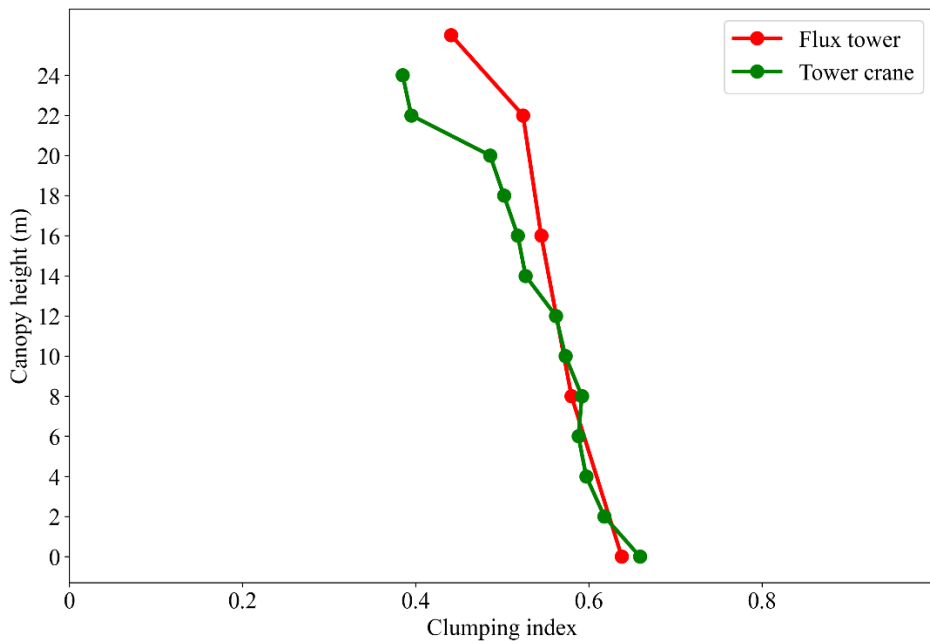


Fig. 28 The vertical profiles of CI at the flux tower and tower crane plots in September 2022.

Fig. 28 compares the vertical CI profile at two plots. CI gradually decreased from the ground to the canopy top at both plots. CI is similar at both plots below 16 m. The CI value decreases sharply from 20 m to 24 m.

5.2.3 May 2023

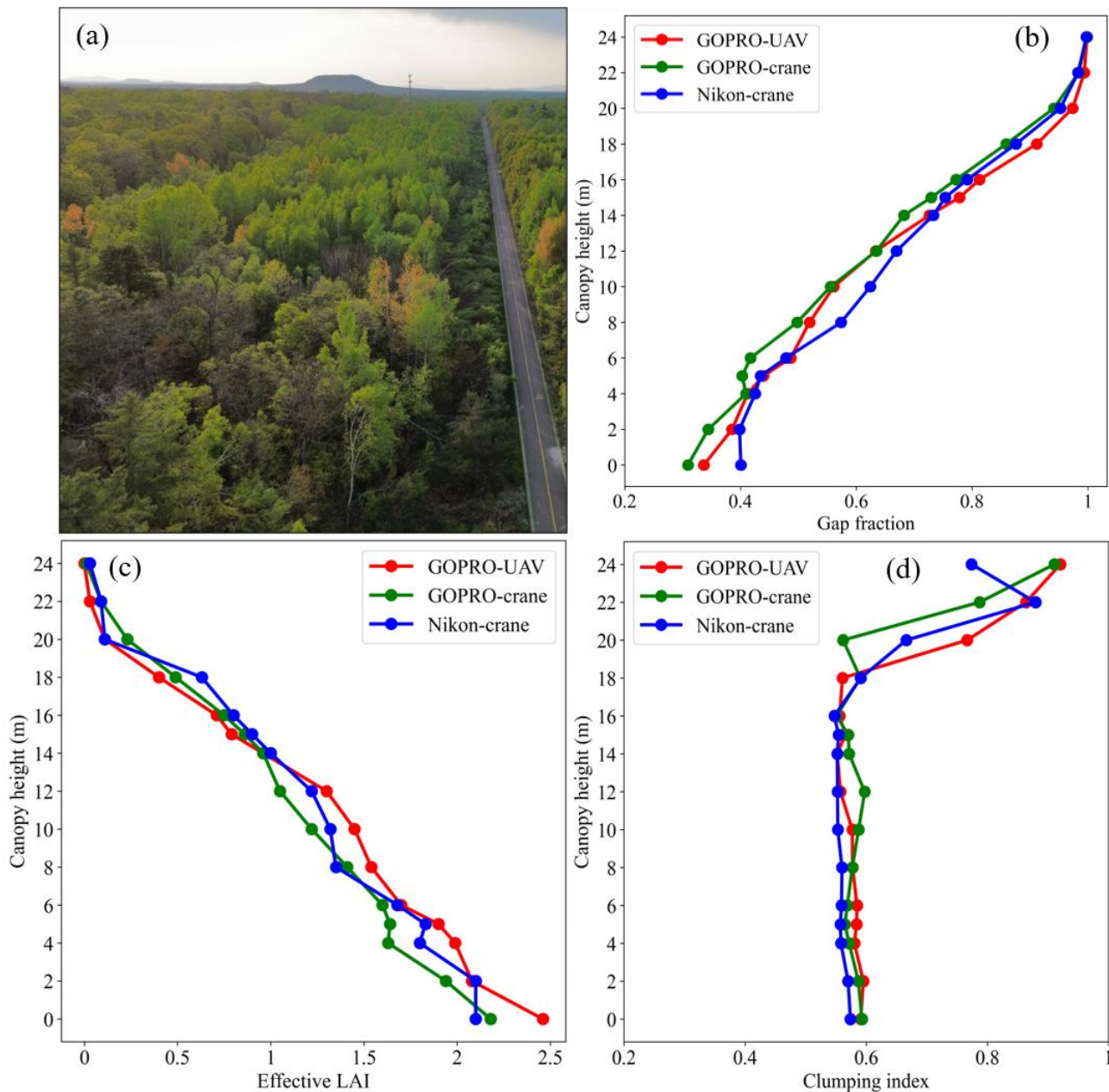


Fig. 29 UAV photo of the measurement site (a), and vertical profiles of gap fraction (b), effective PAI (c), CI (d) in May 2023.

Fig. 29 shows the vertical structural profiles obtained by three different sampling strategies at CBM in May 2023 (leaf-on season, Fig. 29a). Overall, the results obtained by the three sampling strategies are highly consistent. Gap fraction values obtained by the tower crane equipped with the GoPro camera and the UAV equipped with the GoPro camera are the most similar, but the results obtained by the NIKON camera are relatively higher, which may be due to the relatively lower NIKON resolution and its poor ability to distinguish canopy gaps. The  $PAI_{eff}$  deviation measured by the UAV + GoPro DHP is relatively larger than the other two methods, which is mainly due to the height error caused by the UAV's inner GPS.

### 5.2.4 September 2023

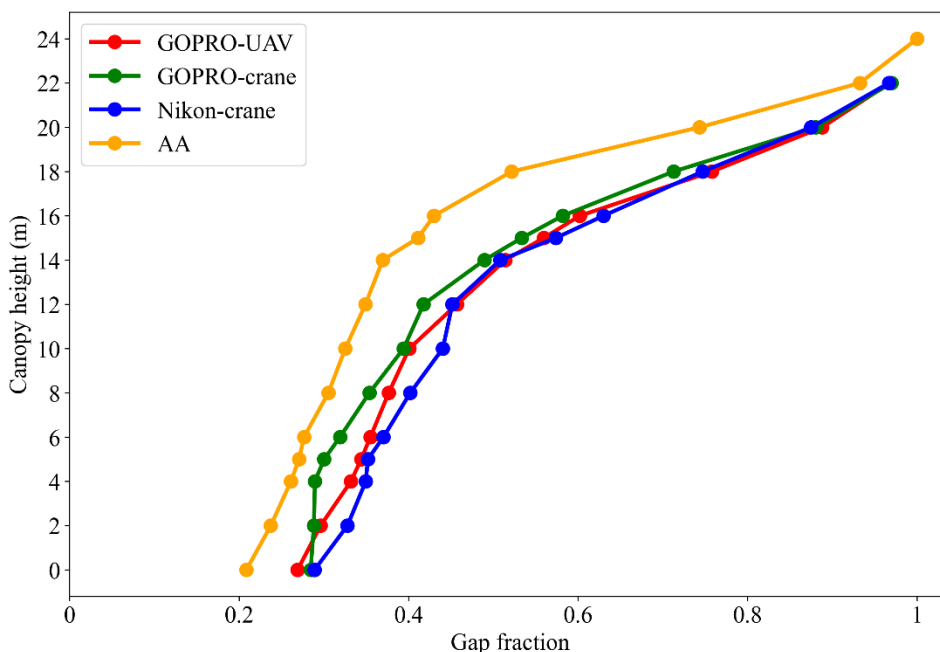


Fig. 30 The vertical profiles of gap fraction at the tower crane and AA plots in September 2023.

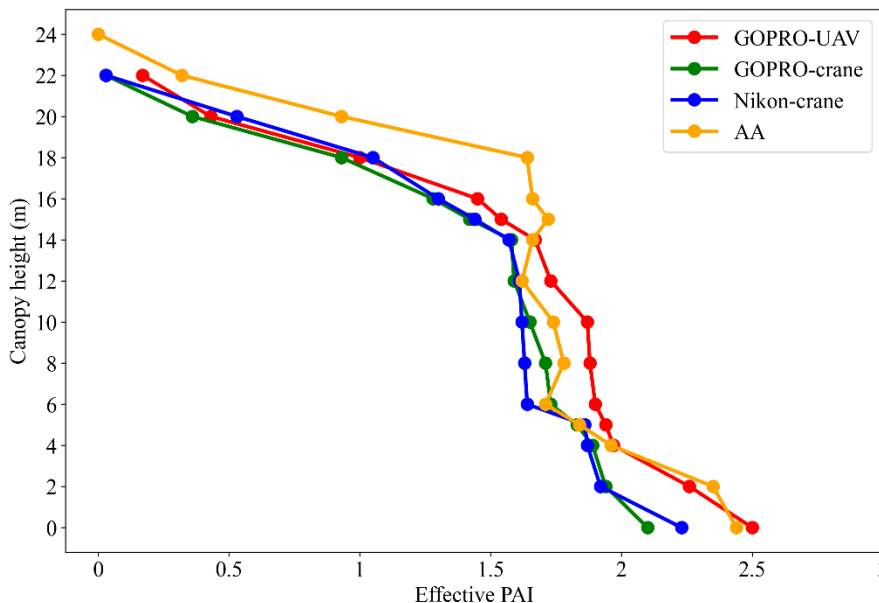


Fig. 31 The vertical profiles of effective PAI at the tower crane and AA plots in September 2023.

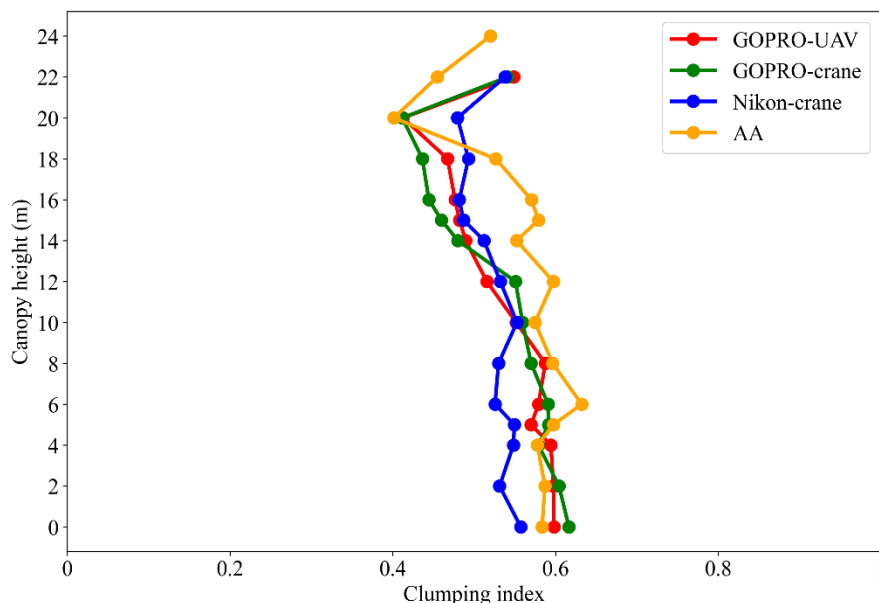


Fig. 32 The vertical profiles of CI at the tower crane and AA plots in September, 2023.

Fig. 30-32 show the vertical structural profiles obtained by three different sampling strategies at CBM in September 2023. The profiles obtained by the three measurement strategies at the tower crane plot are highly consistent. The gap fraction measured by UAV + GOPRO DHP is slightly lower than those of the other two strategies at 0 m (Fig. 30). This is because the tower crane + DHP method fixes DHP cameras on the tower crane hook, and the hook is about 1.5m from the ground, whereas the UAV takes pictures starting from 0 m. As the height increases, the results of the three measurement methods

become more and more consistent. The gap fraction profile of AA is smaller than that of the tower crane plot.

The UAV + GOPRO  $PAI_{eff}$  slightly overestimates the other two methods at  $<12$  m, mainly due to the height measurement error caused by the UAV's inner GPS. The  $PAI_{eff}$  values of the two plots varied most in the understory and the top of the canopy, mainly because the leaves are concentrated at the understory and canopy top (Fig. 31).

The CI values of the two plots are relatively consistent. The CI value is about 0.6 at 0 m, decreasing with the increase of height, but increasing from 20 m to the canopy top (Fig. 32).

## 6. Quality assurance

The two experimental sites are very flat. The SHB site has a mean altitude of 1584 m and the CBM site ranges from 777 m to 778 m. The DHP was strategically positioned beneath a clear forest window to avoid possible blocking in the camera movement. This placement introduces a potential impact on the estimation of canopy structural parameters from DHP images. In the measurement, DHP images were predominantly collected under diffuse radiation conditions. For the data at the same height within the same plot, they were spatially averaged to estimate the parameters. Note that the data quality was relatively low in June 2021 because certain photos were taken under direct illumination. The number of DHP images at flux towers is limited because DHP can only be placed in one direction at some heights.

Similarly, at the CBM site, at least 4 photos were taken at each direction and height of the flux tower. At the tower crane plot, 16 vertical measurement points were located evenly around the crane. All photos taken at the same height were processed with CAN-EYE. To address potential obstructions, areas in the photos blocked by substantial objects such as the tower and hook were masked.

It is important to recognize that parameter estimation is not only influenced by the image data quality and CAN-EYE settings but also by the classification processes. In the classification, an operator manually determines the plants and backgrounds.

## 7. Data access and citation

### 7.1 Data access

All final results, including CC PAI, PAI<sub>eff</sub>, gap fraction, and CI over each plot can be provided.

Please contact the PI below for the field measured and the processed data.

Prof. Hongliang Fang

LREIS, Institute of Geographic Sciences and Natural Resources Research

Chinese Academy of Sciences (CAS)

11A Datun Road

Beijing, 100101, China

Tel: (8610) 64888055

Fax: (8610) 64889630

Email: [fanghl@lreis.ac.cn](mailto:fanghl@lreis.ac.cn)

### 7.2 Citation

Fang, H., Li, Y., Li, S., Wang, Y., Ma, T., Wu, Y., & Guo, K. (2023). Three-Dimensional Forest Biophysical Measurement in Northern China (ForBio\_3D 2020-2023). Field Measurement Report. Institute of Geographic Sciences and Natural Resources Research, Chinese Academy of Sciences.

## References

- Armston, J., Denham, R., Danaher, T., Scarth, P. and Moffiet, T., 2009. Prediction and validation of foliage projective cover from Landsat-5 TM and Landsat-7 ETM+ imagery. *Journal of Applied Remote Sensing*, 3(1): 033540.
- Baret, F. et al., 2007. LAI, fAPAR and fCover CYCLOPES global products derived from VEGETATION: Part 1: Principles of the algorithm. *Remote Sensing of Environment*, 110(3): 275-286.
- Bera, D., Das Chatterjee, N., Bera, S., Ghosh, S. and Dinda, S., 2023. Comparative performance of Sentinel-2 MSI and Landsat-8 OLI data in canopy cover prediction using Random Forest model: Comparing model performance and tuning parameters. *Advances in Space Research*, 71(11): 4691-4709.
- Bergen, K.M. et al., 2009. Remote sensing of vegetation 3-D structure for biodiversity and habitat: Review and implications for lidar and radar spaceborne missions. 114(G2).
- Brüllhardt, M., Rotach, P., Schleppi, P. and Bugmann, H., 2020. Vertical light transmission profiles in structured mixed deciduous forest canopies assessed by UAV-based hemispherical photography and photogrammetric vegetation height models. *Agricultural and Forest Meteorology*, 281.
- Chen, J.M. and Black, T.A., 1992a. DEFINING LEAF-AREA INDEX FOR NON-FLAT LEAVES. *Plant Cell and Environment*, 15(4): 421-429.
- Chen, J.M. and Black, T.A., 1992b. FOLIAGE AREA AND ARCHITECTURE OF PLANT CANOPIES FROM SUNFLECK SIZE DISTRIBUTIONS. *Agricultural and Forest Meteorology*, 60(3-4): 249-266.
- Detto, M., Asner, G.P., Muller-Landau, H.C. and Sonnentag, O., 2015. Spatial variability in tropical forest leaf area density from multireturn lidar and modeling. *Journal of Geophysical Research-Biogeosciences*, 120(2): 294-309.
- Dubayah, R. et al., 2020. The Global Ecosystem Dynamics Investigation: High-resolution laser ranging of the Earth's forests and topography. *Science of Remote Sensing*, 1: 100002.
- Dutta, D. et al., 2017. Characterizing Vegetation Canopy Structure Using Airborne Remote Sensing Data. *Ieee Transactions on Geoscience and Remote Sensing*, 55(2): 1160-1178.
- Fang, H., 2021. Canopy clumping index (CI): A review of methods, characteristics, and applications. *Agricultural and Forest Meteorology*, 303.
- Fang, H., Baret, F., Plummer, S. and Schaeppman-Strub, G., 2019. An Overview of Global Leaf Area Index (LAI): Methods, Products, Validation, and Applications. *Reviews of Geophysics*, 57(3): 739-799.
- Fang, H., Ye, Y., Liu, W., Wei, S. and Ma, L., 2018. Continuous estimation of canopy leaf area index (LAI) and clumping index over broadleaf crop fields: An investigation of the PASTIS-57 instrument and smartphone applications. *Agricultural and Forest Meteorology*, 253-254: 48-61.
- Garrigues, S., Lacaze, R., Baret, F., Morisette, J.T. and Yang, W.J.J.o.G.R.A., 2008. Validation and intercomparison of global Leaf Area Index products derived from remote sensing data, *Journal of Geophysical Research*. 113, G02028(G2): doi:10.1029/2007JG000635.

- Gastellu-Etchegorry, J.P., Demarez, V., Pinel, V. and Zagolski, F., 1996. Modeling radiative transfer in heterogeneous 3-D vegetation canopies. *Remote Sensing of Environment*, 58(2): 131-156.
- Gonsamo, A., D'odorico, P. and Pellikka, P., 2013. Measuring fractional forest canopy element cover and openness – definitions and methodologies revisited. 122(9): 1283-1291.
- Jennings, S., Brown, N. and Sheil, D., 1999. Assessing forest canopies and understorey illumination: canopy closure, canopy cover and other measures. *Forestry: An International Journal of Forest Research*, 72(1): 59-74.
- Lang, A.R.G. and Yueqin, X., 1986. Estimation of leaf area index from transmission of direct sunlight in discontinuous canopies. *Agricultural and Forest Meteorology*, 37(3): 229-243.
- Li, L. et al., 2023. Review of ground and aerial methods for vegetation cover fraction (fCover) and related quantities estimation: definitions, advances, challenges, and future perspectives. *ISPRS-J. Photogramm. Remote Sens.*, 199: 133-156.
- Liu, Y., Liu, R. and Chen, J.M., 2012. Retrospective retrieval of long-term consistent global leaf area index (1981–2011) from combined AVHRR and MODIS data. 117(G4).
- Lovell, J.L., Jupp, D.L.B., Culvenor, D. and Coops, N.C., 2003. Using airborne and ground-based ranging lidar to measure canopy structure in Australian forests. *Can. J. Remote Sens.*, 29: 607 - 622.
- Ma, L. et al., 2018. Retrieving forest canopy clumping index using terrestrial laser scanning data. *Remote Sensing of Environment*, 210: 452-472.
- McManamon, P., 2019. *LiDAR Technologies and Systems*.
- Morsdorf, F. et al., 2010. Discrimination of vegetation strata in a multi-layered Mediterranean forest ecosystem using height and intensity information derived from airborne laser scanning. *Remote Sensing of Environment*, 114(7): 1403-1415.
- Nilson, T., 1971. A theoretical analysis of the frequency of gaps in plant stands. *Agricultural Meteorology*, 8: 25-38.
- Parker, G.G., Lefsky, M.A. and Harding, D.J., 2001. Light transmittance in forest canopies determined using airborne laser altimetry and in-canopy quantum measurements. *Remote Sensing of Environment*, 76(3): 298-309.
- Pisek, J., Lang, M., Nilson, T., Korhonen, L. and Karu, H., 2011. Comparison of methods for measuring gap size distribution and canopy nonrandomness at Järvelja RAMI (RAdition transfer Model Intercomparison) test sites. *Agricultural and Forest Meteorology*, 151(3): 365-377.
- Qi, J. et al., 2019. LESS: LargE-Scale remote sensing data and image simulation framework over heterogeneous 3D scenes. *Remote Sensing of Environment*, 221: 695-706.
- Shugart, H.H., Saatchi, S. and Hall, F.G., 2010. Importance of structure and its measurement in quantifying function of forest ecosystems. *Journal of Geophysical Research: Biogeosciences*, 115(G2).
- Simioni, G., Marie, G. and Huc, R., 2016. Influence of vegetation spatial structure on growth and water fluxes of a mixed forest: Results from the NOTG 3D model. *Ecological Modelling*, 328: 119-135.
- Stenberg, P., Mottus, M., Rautiainen, M. and Sievanen, R., 2014. Quantitative characterization of clumping in Scots pine crowns. *Ann Bot*, 114(4): 689-94.

- Tang, H. and Armston, J., 2019. Algorithm Theoretical Basis Document (ATBD) for GEDI L2B Footprint Canopy Cover and Vertical Profile Metrics. In: C.P. University of Maryland, MD (Editor).
- Tang, H., Dubayah, R., Brogly, M., Ganguly, S. and Zhang, G., 2014. Large-scale retrieval of leaf area index and vertical foliage profile from the spaceborne waveform lidar (GLAS/ICESat). *Remote Sensing of Environment*, 154: 8-18.
- Tang, H. et al., 2012. Retrieval of vertical LAI profiles over tropical rain forests using waveform lidar at La Selva, Costa Rica. *Remote Sensing of Environment*, 124: 242-250.
- Wang, Y. and Fang, H., 2020. Estimation of LAI with the LiDAR Technology: A Review. *Remote Sensing*, 12(20).
- Wei, S., Fang, H., Schaaf, C.B., He, L. and Chen, J.M., 2019. Global 500 m clumping index product derived from MODIS BRDF data (2001–2017). *Remote Sensing of Environment*, 232: 111296.
- Weiss, M. and Baret, F., 2017. CAN-EYE V6.4.91 USER MANUAL, [https://www6.paca.inrae.fr/can-eye/content/download/3052/30819/version/4/file/CAN\\_EYE\\_User\\_Manual.pdf](https://www6.paca.inrae.fr/can-eye/content/download/3052/30819/version/4/file/CAN_EYE_User_Manual.pdf).
- Weiss, M. et al., 2004. Review of methods for in situ leaf area index (LAI) determination: Part II. Estimation of LAI, errors and sampling. *121(1-2): 37-53*.
- Zeng, W. and Wang, W., 2015. Combination of nitrogen and phosphorus fertilization enhance ecosystem carbon sequestration in a nitrogen-limited temperate plantation of Northern China. *Forest Ecology and Management*, 341: 59-66.
- Zheng, G. et al., 2017. Retrieving Directional Gap Fraction, Extinction Coefficient, and Effective Leaf Area Index by Incorporating Scan Angle Information From Discrete Aerial Lidar Data. *IEEE Transactions on Geoscience and Remote Sensing*, 55(1): 577-590.